JPhys Materials

TOPICAL REVIEW • OPEN ACCESS

Interphases in the electrodes of potassium ion batteries

To cite this article: Yupei Han *et al* 2022 *J. Phys. Mater.* **5** 022001

IOP Publishing J. Phys. Mater. 5 (2022) 022001 https://doi.org/10.1088/2515-7639/ac5dce

Journal of Physics: Materials

OPEN ACCESS

RECEIVED
7 December 2021

REVISED
1 March 2022

ACCEPTED FOR PUBLICATION
15 March 2022

PUBLISHED
29 March 2022

TOPICAL REVIEW

Interphases in the electrodes of potassium ion batteries

Yupei Han, Ajay Piriya Vijaya Kumar Saroja, Henry R Tinker and Yang Xu*

Department of Chemistry, University College London, 20 Gordon Street, London WC1H 0AJ, United Kingdom
* Author to whom any correspondence should be addressed.

E-mail: y.xu.1@ucl.ac.uk

Keywords: interphase, potassium ion battery, solid-electrolyte interphase, cathode-electrolyte interphase, heterostructure, reaction kinetics, charge transfer

Abstract

Rechargeable potassium-ion batteries (PIBs) are of great interest as a sustainable, environmentally friendly, and cost-effective energy storage technology. The electrochemical performance of a PIB is closely related to the reaction kinetics of active materials, ionic/electronic transport, and the structural/electrochemical stability of cell components. Alongside the great effort devoted in discovering and optimising electrode materials, recent research unambiguously demonstrates the decisive role of the interphases that interconnect adjacent components in a PIB. Knowledge of interphases is currently less comprehensive and satisfactory compared to that of electrode materials, and therefore, understanding the interphases is crucial to facilitating electrode materials design and advancing battery performance. The present review aims to summarise the critical interphases that dominate the overall battery performance of PIBs, which includes solid-electrolyte interphase, cathode-electrolyte interphase, and solid–solid interphases within composite electrodes, via exploring their formation principles, chemical compositions, and determination of reaction kinetics. State-of-the-art design strategies of robust interphases are discussed and analysed. Finally, perspectives are given to stimulate new ideas and open questions to further the understanding of interphases and the development of PIBs.

1. Introduction

Global efforts towards minimising carbon emissions and promoting carbon neutrality have led to a decrease in conventional fossil fuel usage and the development of cost-effective sustainable energy [1, 2]. In this regard, electrochemical energy storage systems with net-zero carbon emissions have drawn considerable attention [3, 4]. Owing to high energy density and mature industrial manufacturing, lithium-ion batteries (LIBs) are the most extensively used method of rechargeable energy storage, found in electric vehicles, portable electronic devices, and grid energy storage [5–7]. However, low lithium reserves (0.0017 wt%) in the Earth's crust, coupled with rapidly rising depletion and an imbalanced geographical distribution, raise concerns about the sustainable development and long term future of LIBs [8]. As alternatives to LIBs, other alkali metal ion batteries such as sodium-ion batteries (SIBs) and potassium-ion batteries (PIBs) have been extensively studied due to similar electrochemical properties of these alkali metals and high abundancies of Na (2.36 wt%) and K (2.09 wt%) [9]. With a comparable abundance to Na, K possesses an advantage in redox potential. In aqueous electrolytes, K^+/K has a redox potential of −2.93 V versus the standard hydrogen electrode, being lower than that of Na^+/Na (−2.71 V) [10]. In organic electrolytes, the redox potential of K^+/K is even lower than those of both Li and Na by 0.09 and 0.23 V, respectively [11, 12]. Moreover, a solvated K-ion has a smaller Stokes radius due to its weaker Lewis acidity compared to Li- and Na-ions, which translates to a lower desolvation energy at an electrode/electrolyte interface, contributing to a high ionic conductivity of K electrolytes [13]. It is worth emphasising that K-ions can be electrochemically intercalated into graphite, the commercial anode in LIBs, to form KC_8 with a theoretical capacity of 279 mAh g^{-1}, offering the industrial basis for the commercialisation of PIBs.

The past 5 years have seen extensive research activities around the electrode materials of PIBs. This has resulted in a diverse range of feasible cathode and anode materials for PIBs, which has been nicely

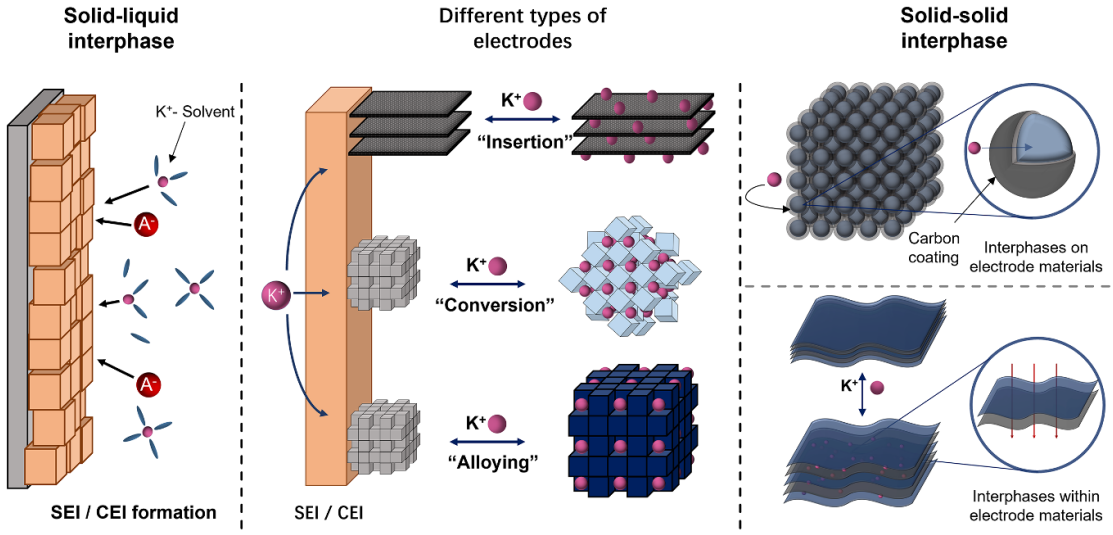

Schematic 1. Illustration of the solid–liquid and solid–solid interphases discussed in this review.

summarised in a number of review articles [14–17]. Alongside the research progression of electrode materials, it has become undoubtedly imperative that interphases play an equally critical role as electrode materials in determining PIB performance, because interphases affect not only ionic migration and charge transfer but also the structural and electrochemical stability of adjacent material phases interconnected by the interphases [18, 19]. These fundamental impacts are often reflected nominally by the rate capability, coulombic efficiency, and cyclability of PIBs [20].

Various types of interphases are presented in a PIB cell (schematic 1). On the anode side, the solid-electrolyte interphase (SEI) forms on the anode surface by the electrolytic decomposition of electrolyte solvents and salts, being one of the most crucial elements to determine cell performance [21]. Therefore, the formation of a stable SEI layer is the prerequisite for the proper functioning of the anode and a key criterion for the selection of a suitable electrolyte as well. An unstable SEI inevitably leads to continuous electrolyte consumption, structural degradation of the anode, and accumulation of thick and pulverised deposits on the anode surface [22, 23]. In addition, the ionic conductivity of the SEI is very important since SEI behaves as an ionic exchange bridge between the electrolyte and the anode. Because SEI formation originates from electrolyte decomposition, the composition of the SEI is closely related to that of the electrolyte. Research has proven that all aspects of an electrolyte, including inorganic salt, organic solvent, additive, and electrolyte concentration, determine the composition of the SEI, and more inorganic components than organic components in the SEI are considered favourable for PIBs [24, 25]. Inorganic compounds are versatile potassium salts such as KF, K_2CO_3, K_2SO_4 and K_2S, while organic compounds are commonly polyesters (RO–COOK) and polyethers (RO–K). Structural stability of the SEI is susceptible to the higher solubility of organic compounds in the electrolyte [26]. Additionally, with much larger Young's moduli than organic polymeric components, the rigid and robust inorganic compounds can provide further mechanical support on the anode surface. Experiments observed more stable cycling of PIBs with the SEI rich in inorganic compounds [27–31]. On the cathode side, protective cathode electrolyte interphase (CEI), is also formed due to electrolyte decomposition [32]. Similar to the SEI, stability and ionic conductivity are the main criteria for discerning an advantageous CEI. For a high-voltage PIB, the cathode is more vulnerable to the aggressive reactions occurring in its highly oxidative surroundings, thus necessitating a strong CEI, either pristinely or artificially formed, to protect the cathode from the attack of the electrolyte [33, 34]. Furthermore, within an electrode, especially a composite electrode, interphases that interconnect the active material phases and/or the conductive network are as important as an SEI and a CEI, because electronic transport and ionic migration occur at these interphases. It is essential for active material phases that undergo a large volume change during battery cycling to have a robust interfacial connection with the conductive network in order to avoid the loss of electronic connection and the resulting performance degradation [35, 36]. Moreover, chemical coupling between the active material and coating layer can adsorb a large number of K-ions and decrease the K-ion migration barrier, thus facilitating charge transfer at the interphase between the material and the coating layer. For heterojunction active materials, the heterojunction interphases can result in synergistic effects such as rich phase boundaries and vacancies as well as a built-in electric field, which can considerably accelerate charge transport. A large amount of phase boundaries and vacancies can lead to the

formation of defects that offer capacitive active sites with facile ion transport pathways for K-ion storage [37]. A built-in electric field can fasten the movement of ions due to electrostatic force, overcoming high energy barriers of K-ion migration when passing through the interphase. More interestingly, the direction of the built-in electric field can alter during charging and discharging processes due to (de)potassiation of active materials, thereby constantly favouring ion transport [37–39].

In this review, we focus on the recent research progress on the investigation of the key interphases present in PIBs. We first start with SEI and CEI, the two solid–liquid interphases, and discuss the role of SEI and CEI in determining the electrochemical performance of PIBs, as well as the strategies to form robust SEI and CEI in PIBs. We then discuss the solid–solid interphases present between the components in composite anodes and cathodes, including the interphase between an electrochemically active material and conductive network and the interphase between two active materials. An emphasis is placed on the benefit of interphases originating from the synergy between the two components. Lastly, we provide concluding perspectives to signpost research directions associated with the interphases in PIBs, that have not been sufficiently explored but are important and worth being fully investigated.

2. SEI

SEI is formed by the reduction of electrolytes on the anode surface, where the decomposition of solvents and salts forms organic and inorganic components [21, 40, 41]. The protective SEI layer avoids further reactions between the electrolyte and the anode, which prevents the continuous consumption of the electrolyte. However, a pristine SEI in PIBs tends to be unstable due to repeated structural fracture during cycling and the solvation of SEI components into the electrolyte, causing the growth into a thick SEI and capacity fading [42–44]. A variety of methods have been proposed to form a durable and robust SEI. The most used strategies include engineering salts and solvents, preconditioning SEI, and redirecting SEI formation.

2.1. SEI regulation with electrolyte engineering

Electrolyte choice is critical. The structural stability and ionic conductivity of SEI are primarily determined by its composition, which is regulated by the electrolyte [45, 46]. SEI layers formed in incompatible electrolytes are easily breakable when encountered with stresses caused by the volume changes of active materials and dendrite formation. SEI fracture can expose fresh sites for new SEI build-ups and accumulation, leading to impedance increase and structural instability of the anode [23, 47]. Organic electrolytes made of K salts solvated in either ester or ether solvents are being extensively investigated for PIBs, with the focus on testing different combinations of K salts, salt concentrations and organic solvents for stable SEI formation [48–50]. General consideration of the generic characteristics for PIB electrolytes can be drawn based on the reported work so far. (a) For the electrolyte solvent, a lower viscosity is beneficial for a higher ionic conductivity. Viscosities of common solvents range from 0.3 to 3.4 centipoise at room temperature [18]. A high lowest unoccupied molecular orbital (LUMO) energy level and a low highest occupied molecular orbital (HOMO) energy level give rise to high anti-reduction and anti-oxidation stability of solvents. Typically, carbonate solvents such as ethylene carbonate (EC), propylene carbonate (PC), dimethyl carbonate, diethyl carbonate (DEC), ethyl methyl carbonate (EMC) show lower LUMO and HOMO energy levels compared with ether solvents such as dimethoxyethane (DME), diethylene glycol dimethyl ether (DEGDME), tetraethylene glycol dimethyl ether and tetrahydrofuran [18]. (b) For potassium salts, high ionic conductivity and solubility in electrolyte solvents are ideal. Potassium hexafluorophosphate (KPF_6), potassium bis(fluorosulfonyl)imide (KFSI) and potassium bis(trifluoromethylsulfonyl)imide (KTFSI) show superior ionic conductivities compared with potassium tetrafluoroborate (KBF_4), potassium perchlorate ($KClO_4$) and potassium trifluoromethanesulfonate (KCF_3SO_3). KFSI and KTFSI possess the highest solubility in non-aqueous solvents [51]. All the salts show similar LUMO energy levels, while KPF_6 and KBF_4 have the highest HOMO energy [18]. It has been demonstrated that suppressing the decomposition of solvents and increasing the inorganic components of SEI can enhance the robustness of the SEI in PIBs.

Among various K salts, KPF_6 and KFSI have received considerable interest. Ji *et al* first noticed that K can be reversibly inserted into graphite using 0.8 M KPF_6 in EC/DEC electrolyte [52]. KPF_6 based electrolytes are electrochemically stable and can passivate Al foil, but the low solubility of KPF_6 in typical non-aqueous solvents limits its concentration in a range of 0.5–1.5 M and co-decomposition of both salts and solvents leads to organic rich SEI layers [17, 53]. During the initial 20 cycles, the SEI layer showed a 30%–60% increase in the contents of C, P and F elements compared with the initial cycle, indicating the continuous decomposition of both salts and solvents. Furthermore, the K element showed a ∼37% decrease, suggesting a growing content of organic compounds in the SEI over cycling [54]. Although efforts have been made to optimise KPF_6 based electrolytes, low CE prevailed due to the huge volume expansion of graphite and unstable SEI formed due to the presence of both organic and inorganic compounds [55–57]. For instance,

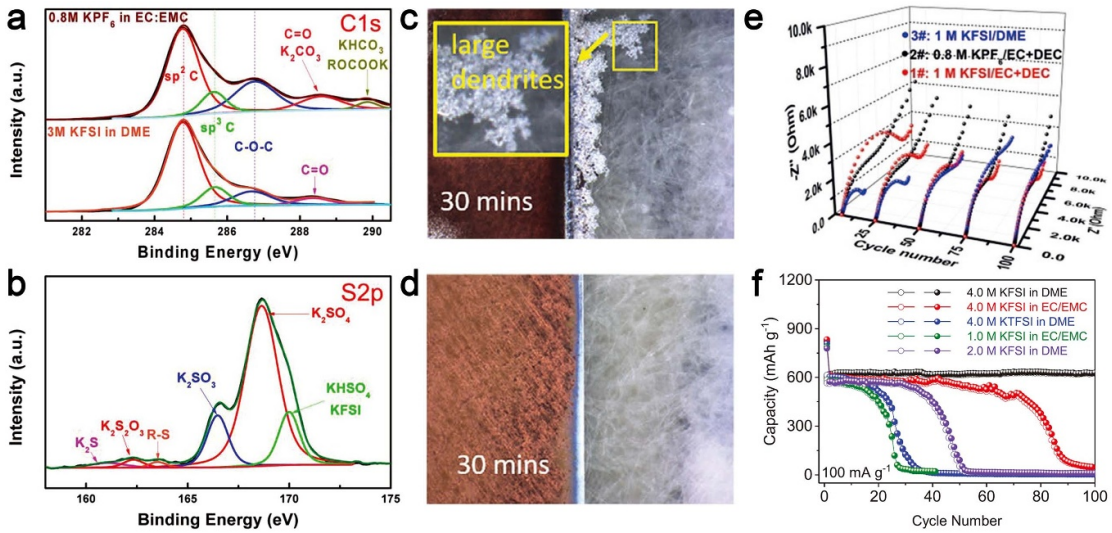

Figure 1. (a), (b) X-ray photoelectron spectroscopy (XPS) spectra of (a) C1s of the carbon anode with two different electrolytes and (b) S2p of the carbon anode with 3 M KFSI in DME electrolyte after 50 cycles. [27] John Wiley & Sons. [© 2018 WILEY-VCH Verlag GmbH & Co. KGaA, Weinheim]. (c), (d) *In situ* optical observations of K metal plating on a Cu substrate in (c) 1 M KFSI/EC:DEC and (d) KFSI/TMP (3:8, molar ratio). [59] John Wiley & Sons. [© 2021 WILEY-VCH Verlag GmbH & Co. KGaA, Weinheim]. (e) Nyquist plots of the PIBs based on amorphous red P/carbon anodes after 5, 25, 50, 75 and 100 cycles. [60] John Wiley & Sons. [© 2019 WILEY-VCH Verlag GmbH & Co. KGaA, Weinheim]. (f) Comparison of the cycling performance of the Sb anodes using different electrolytes at a current density of 100 mA g^{-1}. [61] John Wiley & Sons. [© 2021 WILEY-VCH Verlag GmbH & Co. KGaA, Weinheim].

the SEI layer formed on the surface of carbon using KPF_6 based electrolyte contained K_2CO_3, $KHCO_3$, RO–COOK and RO–K (figure 1(a)) [27]. In contrast, the SEI on carbon using KFSI based electrolytes showed reduced organic components. The decomposition of KFSI formed rich inorganic compounds such as K_2S, $K_2S_2O_3$, K_2SO_3, K_2SO_4 and $KHSO_4$ (figure 1(b)). The SEI layer with increased inorganic components was highly stable, demonstrating excellent cyclic stability of the carbon anode over 14 000 cycles and with a CE of 99.9% [27]. Similarly, inorganic rich SEI has been reported in KFSI based electrolytes for other types of anodes, including intercalation [28, 29], conversion [30] and alloying anodes [31].

For the KFSI based electrolytes, the SEI formation varies with solvent choices. KFSI in the EMC (1:2.5, molar ratio) electrolyte can form a robust SEI on graphite and enable stable cycling for 17 months [58]. However, not all ester carbonates could sustain the long-term cycling of graphite anode. KFSI in EC:DEC electrolyte caused gradual thickening of SEI due to relatively low stability of EC and DEC solvents. This can be alleviated by using more stable DEGDME as the solvent [54]. Moreover, the use of trimethyl phosphate (TMP) can suppress solvent decomposition and form stable SEI [59]. The *in situ* optical views of K metal plating on a Cu substrate demonstrated uneven K plating and the accumulation of K dendrites in 1 M KFSI/EC:DEC (figure 1(c)), but dense and uniform K plating was observed in the KFSI/TMP electrolyte (3:8, molar ratio, figure 1(d)).

For other types of anodes, solvent choice largely depends on the anode material. EC:DEC electrolyte formed a more stable SEI layer on the red P anode compared to DME electrolyte [60]. As shown in figure 1(e), the resistance of the PIB cell with 1 M KFSI/DME continuously increased with cycling, while the resistance remained almost constant after 50 cycles when using 1 M KFSI/EC:DEC, indicating a stable and highly K conductive SEI layer formed on the red P anode. However, DME outperformed ester electrolytes in the case of Sb anode [61]. As shown in figure 1(f), the DME electrolyte offered better cycling performance than the ether electrolyte at various concentrations of KFSI. With concentrated 4 M KFSI in DME electrolyte, the resistance at the interphase even decreased more than 80% after 50 cycles due to suppressed electrolyte decomposition and avoidance of SEI accumulation that is responsible for resistance increase [61]. These results suggest the close dependence among the nature of SEI, the functioning of electrolytes, and the electrochemical reaction of anode materials. Oversimplification should be avoided when looking into the interphase between an anode and an electrolyte to investigate the choice of electrolytes.

In addition to solvent choice, electrolyte concentration plays an important role in SEI formation. Due to the weak solvation of K-ion in triethyl phosphate (TEP), the KFSI/TEP electrolyte demonstrated low viscosity and high conductivity in PIBs, which gave rise to uniform SEI formation in 0.9 M KFSI/TEP, compared to an uneven SEI layer formed in 0.8 M KPF_6/EC:DEC and 1 M KFSI/EC:DEC [62]. More interestingly, an even more uniform SEI was formed when increasing the concentration of KFSI in TEP from

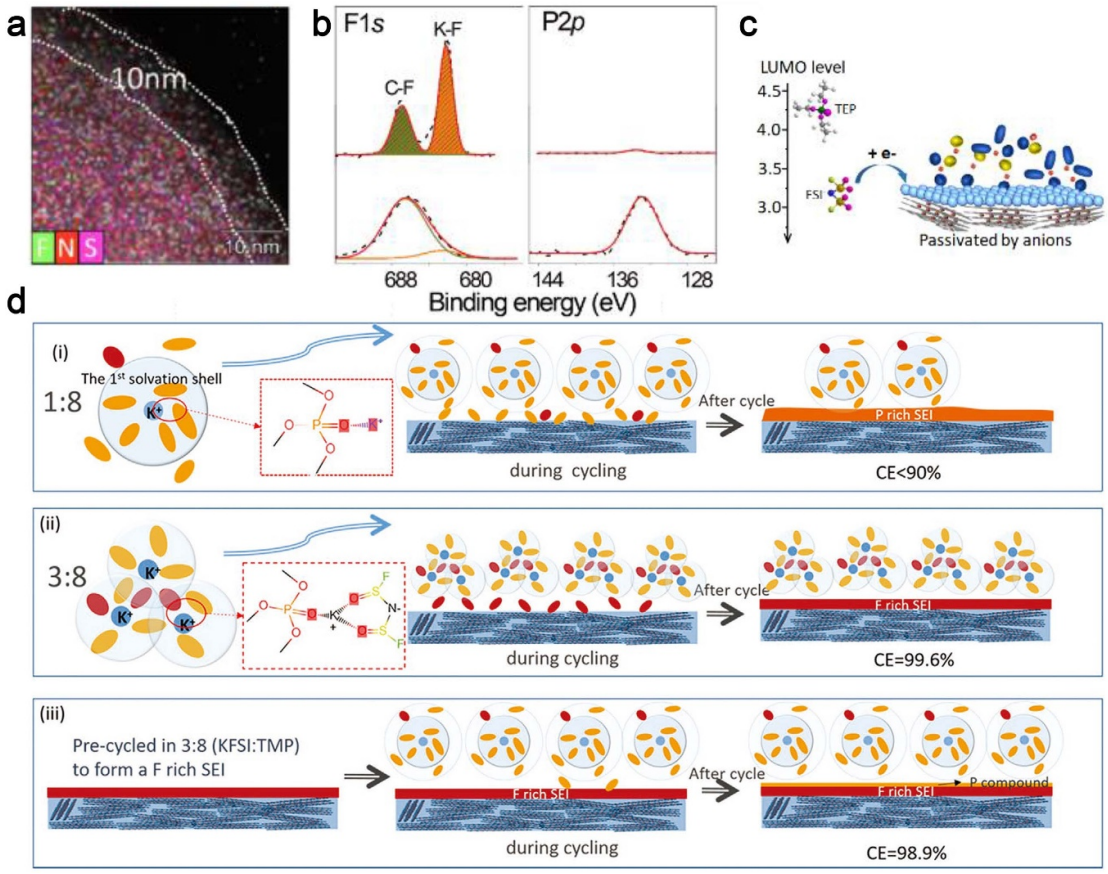

Figure 2. (a) Energy dispersive spectroscopy (EDS) mapping of graphite cycled in 2 M KFSI/TEP for ten cycles; (b) XPS spectra of F 1s and P 2p of the graphite electrode cycled in 2 M KFSI/TEP (top) and 0.9 M KFSI/TEP (bottom); (c) schematic illustration of the SEI formation in 2 M KFSI/TEP passivation. [62] John Wiley & Sons. [© 2020 WILEY-VCH Verlag GmbH & Co. KGaA, Weinheim]. (d) Schematic illustrations of the solvation structure and SEI formation on graphite in (i) KFSI/TMP (1:8, molar ratio) electrolyte and (ii) KFSI/TMP (3:8, molar ratio) electrolyte, respectively. Different solvation structures lead to the P-rich SEI in KFSI/TMP (1:8) and the F-rich SEI in KFSI/TMP (3:8); (iii) a pre-cycled graphite electrode with F-rich SEI was cycled in KFSI/TMP (1:8) electrolyte. The orange and red symbols represent the TMP solvent molecule and the FSI^- anion, respectively. [59] John Wiley & Sons. [© 2021 WILEY-VCH Verlag GmbH & Co. KGaA, Weinheim].

0.9 to 2 M. A thick (∼10 nm) and uniform SEI was formed on the graphite anode after ten cycles of graphite electrodes (figure 2(a)), and the uniformity and stability of the SEI maintained after the following 200 cycles. This was ascribed to the increased decomposition of the FSI^- anions. The x-ray photoelectron spectroscopy (XPS) measurement on the SEI (figure 2(b)) suggested the decomposition of both the solvent and salt at 0.9 M, whereas solvent decomposition was suppressed at 2 M, as indicated by the weak peak of P 2p, and the FSI^- anions became the main source for SEI formation. The simulation results based on the molecular orbital theory [63] showed that in the more concentrated electrolyte the LUMO level of FSI^- was significantly decreased to ∼3.0 eV (figure 2(c)), leading to the preferential decomposition of FSI^- at the graphite surface. Therefore, a uniform and inorganic rich SEI was formed primarily with FSI^- decomposition, which suppressed solvent decomposition and enabled long cyclability.

Electrolyte concentration affects the solvation structure of K-ions as well. It determines the priority of the decomposition reactions of solvents and salts and as a result, regulates the constituents of SEI. Taking the KFSI/TMP electrolyte for an example [59], as shown in figure 2(d)(i), TMP molecules were partially confined within the primary solvation shell of K-ions when the KFSI/TMP molar ratio was 1:8. This gave rise to serious solvent decomposition and irreversible capacity loss during cycling, causing a low CE below 90%. Complete solvation of TMP molecules within the primary solvation shell of K-ions could be achieved when the ratio was raised to 3:8 (figure 2(d)(ii)), which suppressed solvent decomposition and induced anion-derived F-rich SEI to prevent side reactions, offering a CE of 99.6%. Furthermore, when the graphite anode was pre-cycled in the KFSI/TMP (3:8) electrolyte (figure 2(d)(iii)), the anion-derived SEI effectively reduced serious electrolyte decomposition and delivered a CE of 98.9% when subsequently cycled in the KFSI/TMP (1:8) electrolyte. The compatibility of the electrolyte and the F-rich SEI jointly allowed the graphite anode with 74% capacity retention over 2 years of cycling (over 2000 cycles) at 0.2 C. Representative studies of electrolytes for the SEI formation on anode materials are summarised in table 1.

Table 1. Initial CE, cyclability, rate performance, SEI morphology, SEI composition and thickness for different anode materials. Reprinted from [48], Copyright (2021), with permission from Elsevier. Reproduced from [45] with permission from the Royal Society of Chemistry. [60] John Wiley & Sons. [© 2019 WILEY-VCH Verlag GmbH & Co. KGaA, Weinheim]. Reprinted with permission from [46]. Copyright (2021) American Chemical Society. [62] John Wiley & Sons. [© 2020 WILEY-VCH Verlag GmbH & Co. KGaA, Weinheim]. Reprinted from [54], Copyright (2020), with permission from Elsevier.

Anode materials	MoS_2/rGO [48]	—	CoSe–C@C [45]	—	Red P/C [60]	—
Electrolytes	1 M KFSI in EC/PC	1 M KPF_6 in EC/PC	1 M KFSI in EC/DEC	0.8 M KPF_6 in EC/DEC	1 M KFSI in EC/DEC	0.8 M KPF_6 in EC/DEC
Initial CE	∼53%	∼54%	61%	64.5%	—	—
Cyclability	170 at 1 A g^{-1} 500 cycles	111 at 1 A g^{-1} 500 cycles	432 at 0.2 A g^{-1} 1000 cyc.	24 at 0.2 A g^{-1} 200 cyc.	420 at 50 mA g^{-1} 100 cyc.	∼20 at 50 mA g^{-1} 100 cyc.
Rate	196 at 2 A g^{-1}	A little lower	280 at 5 A g^{-1}	80 at 5 A g^{-1}	300, 0.2 A g^{-1}	—
SEI morphology	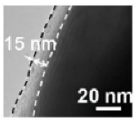	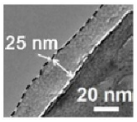	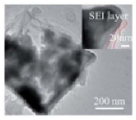	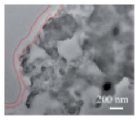	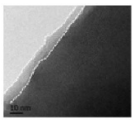	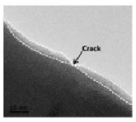
SEI composition	More KF	Organic and inorganic	Rich in KF and K_2SO_4; C–O, C=O, CO_3	K_2CO_3, CH_3OK; C–O, C=O, CO_3	Integrated organic and inorganic	Organic rich
SEI thickness	15 nm	25 nm	∼20 nm	>40 nm	5–10 nm	∼5 nm
Anode materials	Black P/ graphite [46]	—	Graphite [62]	—	Graphite [54]	—
Electrolytes	KFSI/TMP/HFE = 1:1.7:2	5 M KFSI in TMP	2 M KFSI in TEP	1 M KFSI in EC/DEC	0.5 M KPF_6 DEGDME	0.5 M KPF_6 in EC/DEC
Initial CE	∼71%	∼75%	99.7%	∼99%	∼93%	∼66%
Cyclability	342 at 0.3 A g^{-1} 300 cycles	168 at 0.3 A g^{-1} 300 cycles	247 at 0.2 C 300 cycles	∼80 at 0.2 C 180 cycles	80 at 25 mA g^{-1} 50 cycles	50 at 25 mA g^{-1} 50 cycles
Rate	280 at 1 A g^{-1}	190 at 1 A g^{-1}	137 at 2 C	∼10 at 2 C	—	—
SEI morphology	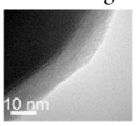	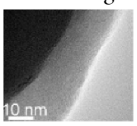	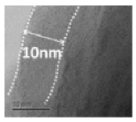	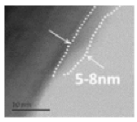	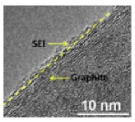	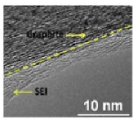
SEI composition	Less KF, K_2S, K_2SO_3; more (S=O)–N	K–F, S–F, (S=O)–N, K_2SO_3, K_2S; C–C, C–OH, C–O, P–O	Rich in inorganic. KF, K_2S, KSON, K_2SO_4, K_2SO_3, S, K_2CO_3, CH_3OK	—	Integrated organic and inorganic	K–F, K–O, C–F, C–O, C–C, C–H, C=O
SEI thickness	9.4 nm	17.7 nm	10 nm	5–8 nm	0.5–1.5 nm	∼5 nm

2.2. Other strategies for a robust SEI

In addition to the regulation of electrolytes, preconditioning is another approach to enhance the robustness of SEI. Preconditioning SEI in a Li-ion containing electrolyte can facilitate K-ion transport through SEI by the progressive substitution of Li-ions with K-ions. This ensures reversible intercalation of K-ions at the anode. Hui *et al* reported stable and fast K-ion intercalation in an ultrathin few-layer graphene (FLG) electrode through preconditioning an SEI in 0.1 M lithium tetrafluoroborate ($LiBF_4$) in EC:PC [64]. As a result, the SEI layer covered uniformly over the entire surface of FLG (figure 3(a)), whereas a patchy SEI layer was formed without the preconditioning. The preconditioned FLG showed reversible intercalation of K-ions for 1000 cycles of cyclic voltammogram (CV) scans (figure 3(b)). Time-of-flight secondary ion mass spectrometry (TOF-SIMS) was used to confirm the existence of both Li- and K-ions and the progressive increase in the K/Li ratio in a preconditioned FLG confirmed the ion exchange between Li- and K-ions (figure 3(c)). This aided the diffusion of K-ions through SEI and facilitated reversible intercalation in FLG.

The growth of SEI can be directed towards high robustness with surface modification of anodes. SEI can be more unstable and thicker on alloying and conversion-based anode materials compared to carbon-based anode materials, because the huge volume change and pulverisation of the former results in the continuous decomposition of electrolytes. Wu *et al* synthesised an ultrathin carbon film@carbon nanorods@Bi nanoparticle (UCF@CNs@BiN) anode, in which the UCF@CN matrix not only accommodated the volume

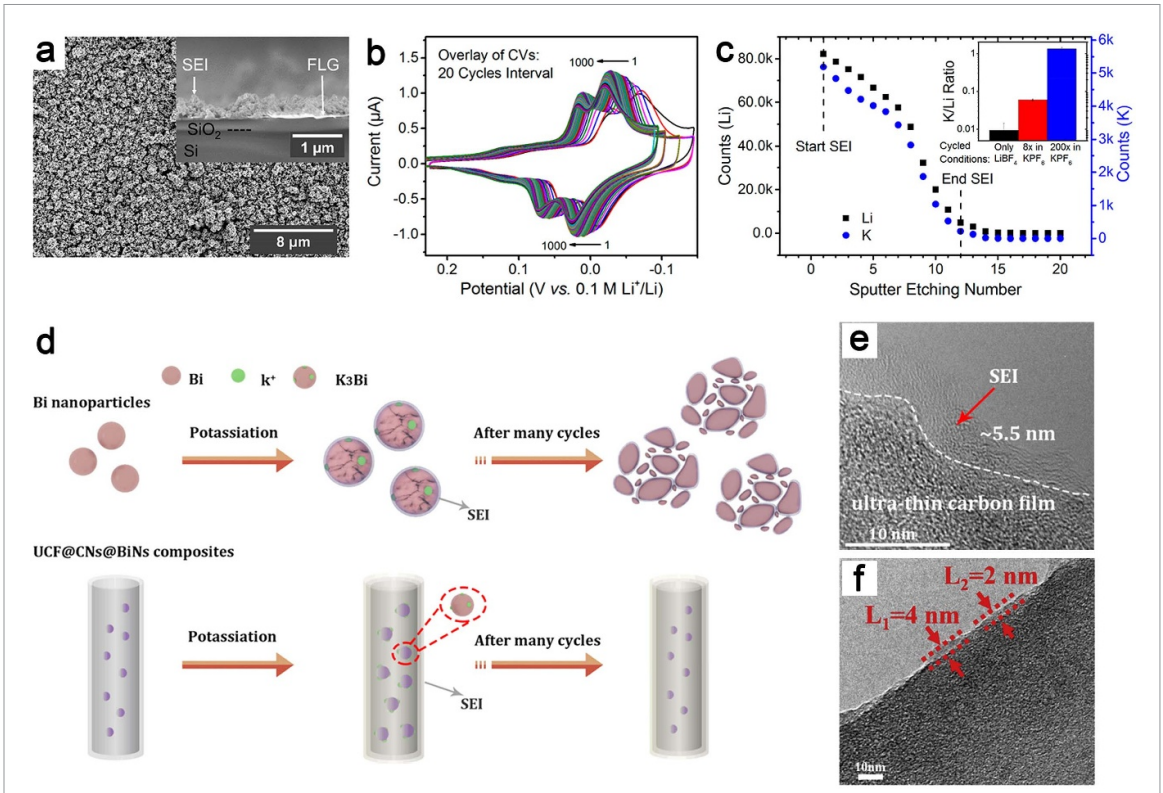

Figure 3. (a) Scanning electron microscope (SEM) image of preconditioned FLG. The inset is the cross-sectional image of the same sample; (b) long-term CV study of the K-ion intercalation in FLG for 1000 cycles at 1 mV s^{-1}; (c) TOF-SIMS depth profiling results of the FLG with full Li-ion based SEI conditioning and exposure to a few cycles in K-ion containing electrolyte. The inset is K/Li counts ratio for the FLG samples under different conditions. Reprinted with permission from [64]. Copyright (2018) American Chemical Society. (d) Schematic illustration of traditional Bi and the UCF@CNs@BiN composite electrode during (de)potassiation process. Reprinted with permission from [65]. Copyright (2019) American Chemical Society. (e) HRTEM image of the UCF@CNs@BiN composite after many cycles. (f) TEM image of P–S co-doped carbon fibre with SiO_2 and MgO nanoparticles after cycling. Reprinted from [66], Copyright (2020), with permission from Elsevier.

change of Bi during potassiation and depotassiation but also directed the SEI formation on carbon matrix rather than on Bi [65]. As shown in figure 3(d), Bi nanoparticles were covered by the SEI layer without the sufficient protection of the carbon film. The SEI layer lost its stability during repeated cycling, due to the expansion and contraction of Bi nanoparticles. This led to the formation of new SEI on the cracked surfaces of Bi nanoparticles. However, the surface modification of Bi particles with UCF@CN matrix redirected the SEI formation on the outer surface of UCF, rather than on the surface of individual Bi nanoparticles, as seen in the high-resolution transmission electron microscope (HRTEM) image (figure 3(e)). The formation of thin (5.5 nm) and stable SEI helped to maintain the structure of Bi even after long cycling. With a very similar approach, the surface modification of carbon anode using inorganic materials impacts the formation of stable SEI. The SiO_2 and MgO nanoparticles distributed in P, S co-doped carbon fibre acted as a seed to adsorb the decomposed electrolyte species and assisted in the formation of an ultrathin SEI (2–4 nm, figure 3(f)) in sharp contrast to the thick SEI (29 nm) without SiO_2 and MgO nanoparticles [66]. An ultrathin SEI layer minimised the charge transfer impedance and reduced the consumption of the electrolyte. The advantages and disadvantages of the strategies discussed in this section are summarised in table 2.

2.3. Advanced characterisation techniques

The chemical composition of SEI has varied proportions of organic and inorganic compounds depending on the salt and solvent used in the electrolyte. Understanding the components of the SEI layer is essential to provide a clear picture of the correlation between cell performance and SEI layer formation. Although XPS is a widely used technique to determine the chemical composition of SEI, the surface-sensitive nature of this technique limits the determination of the compositional distribution in the depth direction. Hence, the combination of XPS and depth profiling with argon ion-beam sputtering is more suitable to provide an in-depth understanding of the distribution of SEI components from surface to bulk. Utilising this technique, Wang *et al* revealed the SEI layer formed on nitrogen-doped graphite foams with KPF_6 and KFSI in EC:DEC electrolytes [44]. The surface of the SEI in KPF_6/EC:DEC electrolyte showed more organic compounds that are rich in oxygen containing species and negligible inorganic compounds such as P–F species from the PF_6^-

Table 2. Advantages and disadvantages of different methods to form SEI layers. Reprinted with permission from [64]. Copyright (2018) American Chemical Society. Reprinted from [66], Copyright (2020), with permission from Elsevier. Reprinted with permission from [65]. Copyright (2019) American Chemical Society.

Methods	Preconditioning the SEI [64]	Blank control	Mitigating SEI growth [65]	Blank control	Redirecting SEI growth [66]
Method description	Pre-forming an SEI layer on the anode in Li^+ containing electrolytes		SiO_2 and MgO nanoparticles in the anode material help form a thin SEI layer		Using a carbon coating as the surface for SEI growth to protect the active material
Anode materials	Few-layer graphene (FLG)		P, S co-doped carbon fibre		Carbon caged Bi particles
SEI morphology	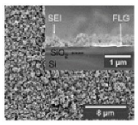	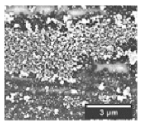	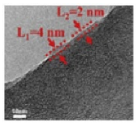	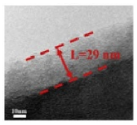	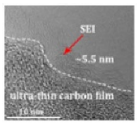 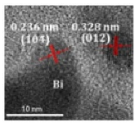
SEI thickness	>200 nm	Patchy surface	2–4 nm	29 nm	~5.5 nm
Pros	Efficient K^+ intercalation		Facilitating charge transfer Facile process		Decreased side reactions Smaller volume changes
Cons	Thick SEI formation Complicated procedure		Moderate cyclability		Low loading of active materials

anion. Ar^+ sputtering for 2 min revealed the existence of inorganic compounds such as KF and P–F along with organic polycarbonates. But the distribution of these inorganic compounds was not uniform and decreased towards the bulk of the SEI layer. Moreover, more oxygen containing carbonates existed on the surface of the SEI rather than in the bulk due to the severe decomposition of the solvent (figure 4(a)). Unlike KPF_6 based electrolytes, the SEI layer formed in KFSI/EC:DEC electrolyte tended to have a lower content of oxygen containing carbonates which were concentrated towards the SEI surface. Meanwhile, the inorganic compound KF was homogeneously distributed throughout the thickness of the SEI layer. In addition, S based inorganic compounds such as K_2SO_3, KSO_2F and $KNSO_2$ also co-existed over the entire SEI layer, enduring stability to the SEI layer.

The use of synchrotron radiation in XPS can provide higher resolution with a high signal-to-noise ratio. Also, XPS of SEI at different depths can be analysed by tuning the energy of excitation radiation without etching out at different depths of the electrode. Naylor *et al* analysed the SEI layer of graphite in KPF_6 EC:DEC electrolyte at different depths of 10, 20 and 50 nm using synchrotron radiation of different excitation energies of 1090, 2150 and 6450 eV, respectively [67]. The surface of the SEI at the depth of 10 nm was rich in organic compounds along with a small proportion of inorganic compounds containing K, F and P. Further increase in the depth of the SEI layer to 20 nm revealed an increased concentration of oxygen containing species. At the depth of 50 nm, inorganic species containing F and P were easy to be found near the bulk of the SEI layer (figure 4(b)).

TOF-SIMS analysis also provides chemical information of SEI layers based on the measurement of mass/electron charge of ejected molecules. The chemical constituents on the top surface of the SEI layer (<10 nm) can be determined using TOF-SIMS with high resolution and sensitivity. The SEI layer of hard carbon anode in the KFSI/PC electrolyte at the depth of 1 nm revealed fewer organic compounds for PIBs than those for LIBs, indicating higher solubilities of the potassium organic compounds such as potassium alkyl carbonates and potassium alkoxides [53].

2.4. SEI related thermal runaway

The safe operation of a battery is indispensable. Safety concerns of PIBs correspond to the formation of pyrophoric KC_8 and the utilisation of inflammable electrolytes, and both can cause exothermal reactions that can lead to thermal runaway and fire hazards. Pol *et al* studied the thermal runaway mechanisms of graphite anodes in PIBs [68]. They compared the differential scanning calorimetry (DSC) curves of fully lithiated and potassiated graphite electrodes. In LIBs, SEI degradation initiated thermal runaway at 110 °C, then followed by the reactions between intercalated Li with the electrolyte solvents, the melting of the $LiPF_6$ salt and the dehydrofluorination of the polyvinylidene difluoride (PVDF) binder (figure 5(a)). In contrast, the PIB began an earlier and more centralised thermal runaway at 100 °C and released a significantly lower total heat of 395 J g^{-1} compared with 1048 J g^{-1} for the LIB. Separated KC_8 particles and electrolytes generated no heat flow unless both were combined (figure 5(b)), which verified that the thermal runaway of K-ion graphite anodes was triggered by the exothermal reactions between directly contacted potassiated graphite and electrolyte due to the degradation of the SEI. During cycling, the significant 60% volume change of the

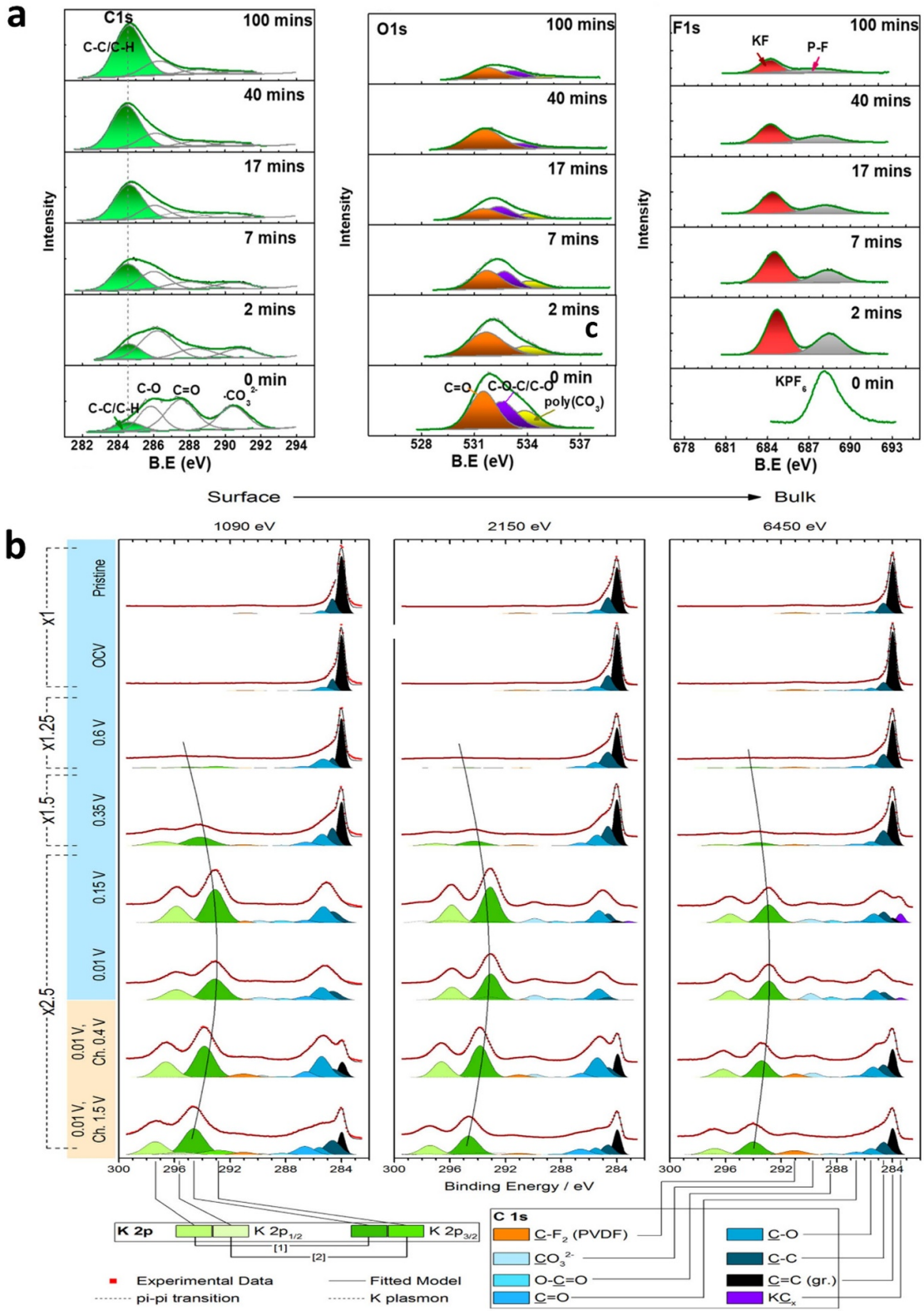

Figure 4. Depth profiling XPS spectra of the SEI layer formed in nitrogen-doped graphitic foam using (a) 0.6 M KPF_6 in EC:DEC. Reprinted with permission from [44]. Copyright (2019) American Chemical Society. (b) C1s and K 2p XPS spectra of SEI layer formed in graphite anode at different probing depths of 10, 20, 50 nm using photon energies of 1090, 2150, 6450 eV respectively. Reprinted with permission from [67]. Copyright (2019) American Chemical Society.

graphite anode induced thick SEI build-ups, which consumed both K-ions and electrolytes. As shown in figure 5(c), because the main sources of thermal runaway were depleted over cycling, the heat release was halved from the first cycle to the 10th cycle and further halved at the 25th cycle. Therefore, a robust SEI layer that prevents exothermal reactions between the electrolyte and potassiated graphite is crucial to mitigate the

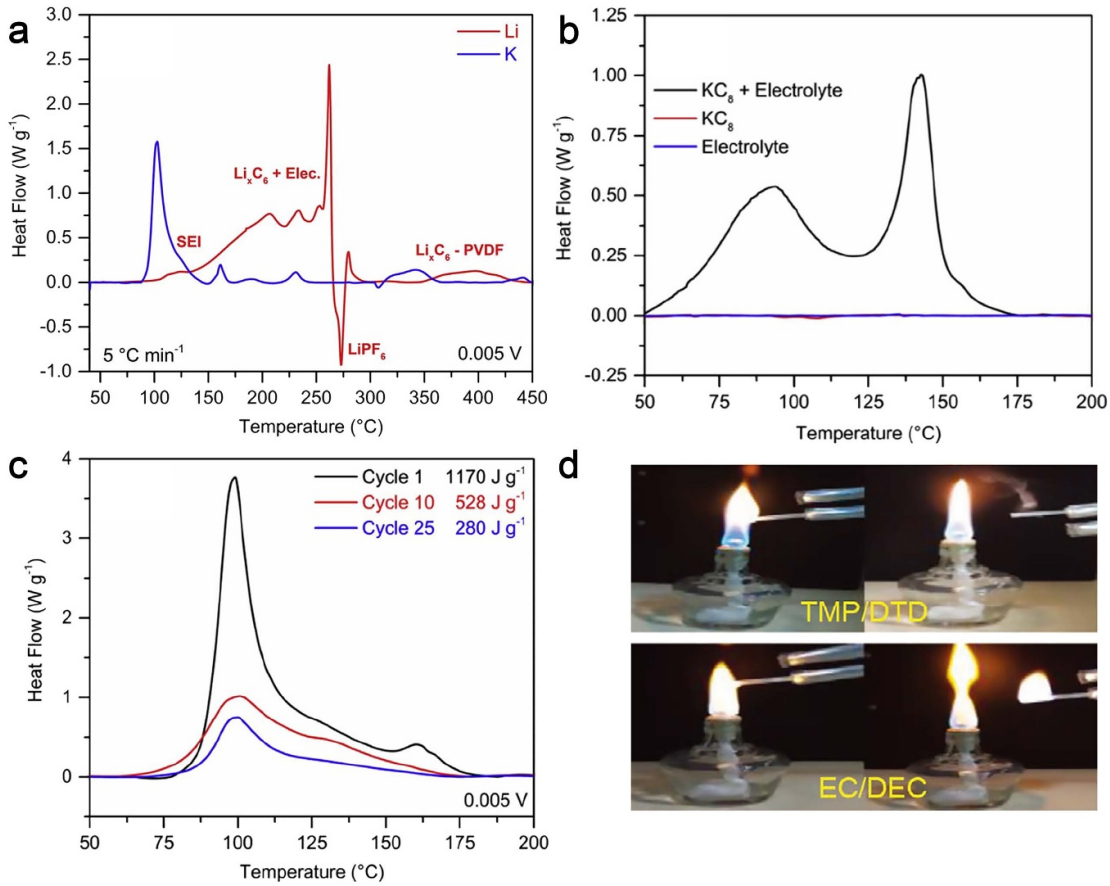

Figure 5. (a) DSC profiles of fully charged graphite electrodes prepared by a Li-ion or K-ion battery configuration, with Li-ion degradation reactions labelled; (b) DSC profiles of chemically synthesised KC_8 with electrolyte; (c) DSC profiles of K-ion graphite electrodes after different numbers of cycles. Reprinted from [68], Copyright (2018), with permission from Elsevier. (d) Flammability test for TMP and EC-DEC based electrolytes. [70] John Wiley & Sons. [© 2020 WILEY-VCH Verlag GmbH & Co. KGaA, Weinheim].

thermal runaway of PIBs. To this end, non-flammable phosphate solvent should have a high priority to improve the safety of PIBs. TEP and TMP solvents are intrinsically non-flammable solvents (figure 5(d)), and a high salt-to-solvent ratio (over 2 M) can help to form robust SEI layers, suppressing thermal runaway [59, 62, 69]. Additionally, the ethylene sulphate additive reduces the workable electrolyte concentration to 1 M in the TMP solvent by impacting the K^+ solvation structure [70].

3. CEI

Similar to SEI, CEI is a protective film formed on the surface of a cathode due to the oxidation of the electrolytes. Stabilisation of CEI within five cycles was revealed from the electrochemical impedance spectroscopy (EIS) measurements (figure 6(a)) [71, 72]. A stable CEI can protect the cathode from the attack of the electrolyte to avoid the structural degradation and pulverisation of the cathode [71, 73]. This protection is crucial for high-voltage cathodes, as aggressive reactions are frequent at a high voltage.

The composition of CEI tightly depends on the electrolyte used and shows high similarities with those of SEI formed in the same electrolyte. The CEI of P2-type $K_{0.44}Ni_{0.22}Mn_{0.78}O_2$ cathode in 0.8 M KPF_6 in EC:DEC was composed of both organic and inorganic compounds [72]. The decomposition of EC and DEC formed potassium alkyl carbonates (RCO_2K), potassium carbonate (K_2CO_3), and potassium alkoxides (KOR) (figure 6(b)). KF was formed either due to the decomposition ($KPF_6 \rightarrow KF + PF_5$) or hydrolysis of KPF_6 ($KPF_6 + H_2O \rightarrow KF + 2HF + OPF_3$) (figure 6(c)). In another case, the CEI formed in 6 M KFSI in diglyme contained inorganic salts (KF, KSON, K_2SO_4, K_2SO_3, and $K_2S_2O_3$) derived from KFSI and organic components (polyether and RCH_2OK) originated from diglyme (figure 6(d)) [74].

The interphase between a cathode and an electrolyte can be evolving during cell cycling and subsequently result in the additional function of the interphase. The interphase layer of P2–$K_{0.67}MnO_2$ (P2–KMO) cathode in 6 M KFSI in diglyme evolved into a dual-layer structure consisting of a CEI and a K-deficient spinel layer [74]. Interestingly, the K-deficient spinel layer with a thickness of 10–30 nm can block the direct

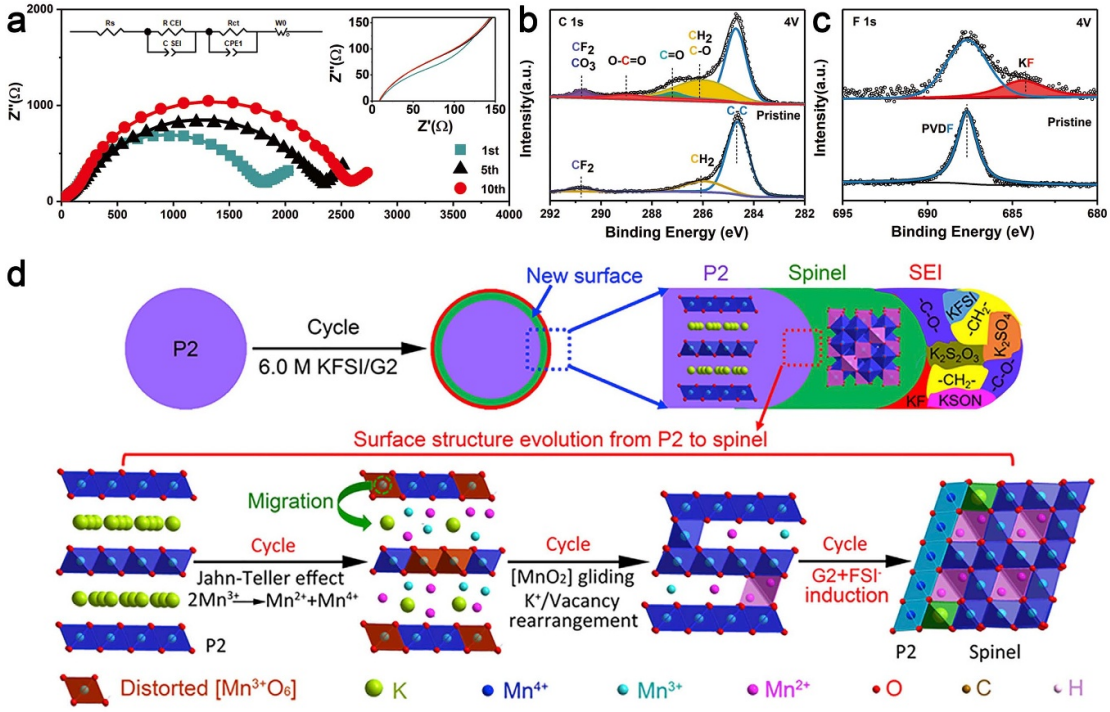

Figure 6. (a) EIS spectra of P2-type $K_{0.44}Ni_{0.22}Mn_{0.78}O_2$ in the charged state after different cycles with the inset of high-frequency semicircles and the equivalent circuit; (b), (c) XPS spectra of (a) C1s and (b) F1s of the pristine and cycled $K_{0.44}Ni_{0.22}Mn_{0.78}O_2$ cathodes. [72] John Wiley & Sons. [© 2019 WILEY-VCH Verlag GmbH & Co. KGaA, Weinheim]. (d) Schematic illustration of the formation of the dual interphase layers in P2–$K_{0.67}MnO_2$. Reprinted from [74], Copyright (2019), with permission from Elsevier.

contact between the electrolyte and P2–KMO. This prevented the further growth of CEI and stabilised the cathode structure. As shown in figure 6(d), the authors suggested three stages for the structure evolution from P2 to spinel. The first stage is the Jahn–Teller distortion and disproportionation of Mn^{3+}, then the gliding of the $[MnO_2]$ layers and rearrangement of K-ions with vacancies occurring, and finally, the spinel phase was formed due to further atomic rearrangement induced by a strong electronegativity of the aggregated FSI^- and adsorption of diglyme.

As a protective interphase layer, a CEI should possess decent rigidity and flexibility as mechanical support to the cathode structure. At the same time, as an ionic bridge interconnecting the cathode and the electrolyte, a CEI adds kinetic hindrances for K-ion transfer and therefore, a thin CEI is considered favourable for fast K-ion transport [71, 75, 76]. A trade-off between mechanical strength and ionic conductivity should be considered in CEI design. Borrowing ideas from the lithium counterpart, engineering the first solvation sheath of K-ions with solvent molecules exerting a lower K binding energy could offer facile desolvation of K-ions and fast interfacial kinetics [77]. Representative studies of CEI formation are summarised in table 3.

4. Interphases in composite anodes

Interphases between two solid material phases in a PIB cell, such as active materials, conductive carbonaceous network, binders, and coating layers, can be treated as solid–solid interphases, in comparison to the solid–liquid interphases previously discussed in the forms of SEI and CEI. Anode materials for PIBs primarily include intercalation-type (e.g. graphite [78]), conversion-type (e.g. metal oxides [79], chalcogenides [80], and phosphides [81]), and alloying-type (e.g. Bi [82] and Sb [83]). Large volume changes usually occur in these materials during K-ion insertion. For example, graphite suffers more than 60% of volume expansion when cycled in carbonate electrolytes [84], and the expansion can be as high as 400% in the case of Bi or Sb [85, 86]. Carbonaceous coating on active materials has been extensively used to accommodate the volume changes during cycling and compensate for the insufficient electronic conductivity of anode materials [87–91]. A surface coating layer forms an interphase on the active material, and the atomic interaction at the interphase can increase the adsorption of K-ions and reduce the energy barriers of K-ion migration. With regard to heterojunction electrodes, built-in electric field and vacancy structures established in the interphases can facilitate ion migration when passing through multiphase transitions.

Table 3. Initial CE, cyclability, rate performance, CEI morphology, CEI composition and thickness for different cathode materials. Reprinted from [74], Copyright (2019), with permission from Elsevier. [72] John Wiley & Sons. [© 2019 WILEY-VCH Verlag GmbH & Co. KGaA, Weinheim]. Reprinted from [75], Copyright (2021), with permission from Elsevier.

Cathode materials	$K_{0.67}MnO_2$ [74]	—	$K_{0.44}Ni_{0.22}Mn_{0.78}O_2$ [72]	Methylene blue [75]	—	—
Electrolytes	6 M KFSI in G2	6 M KFSI in EC/DEC/FEC	0.8 M KPF_6 in EC/DEC	3 M KFSI in DME	1 M KFSI in DME	1 M KFSI in EC/DEC
Initial CE	∼50%	∼58%	87.7%	∼88.9%	—	—
Cyclability	71 at 50 mA g^{-1} 300 cycles	10 at 50 mA g^{-1} 50 cycles	∼59 at 0.2 A g^{-1} 500 cycles	139.5, 0.1 A g^{-1} 500 cyc.	∼20 at 0.1 A g^{-1} 100 cyc.	∼80 at 0.1 A g^{-1} 100 cyc.
Rate	—	—	61.3 at 0.5 A g^{-1}	54 at 10 A g^{-1}	∼27 at 10 A g^{-1}	∼5 at 10 A g^{-1}
CEI morphology	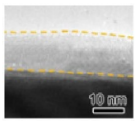	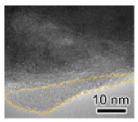	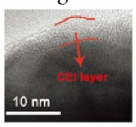	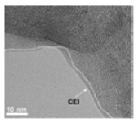	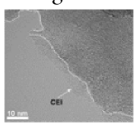	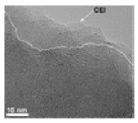
CEI composition	KF, KSON, $K_2S_2O_3$, K_2SO_4, K_2SO_3, polyether, RCH_2OK	KF, RCH_2OK, polyether,	KF, RCO_2K, K_2CO_3, KOR	Inorganic rich. C–F, S–F, K–F	C–F, S–F, K–F	C–F, S–F, K–F
CEI thickness	∼10 nm	2–10 nm	4–5 nm	∼2 nm	∼5 nm	10–20 nm

4.1. Interphases on anode materials

Wang *et al* synthesised $MoSe_2$/C core/shell nanostructures, in which an amorphous carbon shell confined the $MoSe_2$ nanosheets and accelerated electronic transfer along the surface of the carbon (figures 7(a) and (b)) [92]. With the supportive confinement of a thin carbon layer, the volume expansion of $MoSe_2$ was alleviated. A similar carbonaceous coating strategy has been used for other anode materials such as Sn_4P_3, Fe_3C, Bi, Sb and P [93–97]. Jia *et al* prepared MoS_2/N-doped-C hollow tubes with sufficient interior space to mitigate strain and cage the products (polysulphides and Mo nanoparticles) of the conversion reactions, which prevented uncontrollable parasitic reactions [98]. The density functional theory calculations (figures 7(d) and (e)) indicated that the N-doped-C/MoS_2 interphase could strongly bond two K atoms simultaneously, with an adsorption energy of −1.37 eV for each K atom, being higher than −1.29 eV for the MoS_2/MoS_2 interphase, thereby providing an additional attraction towards K atoms and facilitating charge transfer. Strong interfacial chemical coupling has also been proven beneficial by coating MXene on the surface of $MoSe_2$ nanosheets. The coupling promoted charge transfer kinetics and improved the structural durability of the $MoSe_2$/MXene electrode [99]. Wang *et al* synthesised Co_3Se_4 quantum-dots (QDs) to address poor conductivity and huge volume expansion of Co_3Se_4 [100]. The Co_3Se_4 QDs were uniformly embedded in an amorphous N-doped carbon network (figure 7(c)), which prevented the aggregation of the QDs and improved electronic conductivity. During cycling, the volume change of Co_3Se_4 QDs was well confined within the local N-doped carbon network, avoiding increased exposed surfaces for the repeated decomposition of electrolytes. As a result, a stable SEI film was formed on the structure of Co_3Se_4 QDs encapsulated by N-doped carbon, which enabled stable cycling performance over 10 000 cycles at a current density of 1 A g^{-1}.

With abundant active sites, reduced graphene oxide (rGO) exerts strong interfacial interactions with active materials. Wang *et al* proved that the interfacial bonding between metal–organic framework (MOF) nanocrystals and rGO was beneficial for the electrochemical performance, by comparing the adsorption energy (E_{ad}) of K-ions on the Co-MOF-rGO hybrid and Co-MOF/rGO composite that was without chemical bonding [101]. As shown in figure 8(a), Co-MOF-rGO showed an E_{ad} of −2.83 eV, which was higher than that of Co-MOF/rGO (−2.53 eV). Nudged elastic band (NEB) calculations (figures 8(b) and (c)) further demonstrated a lower K-ion diffusion barrier in the Co-MOF-rGO hybrid (0.62 eV) compared to that of Co-MOF/rGO (1.51 eV). Therefore, the strong chemical coupling between rGO and Co-MOF enhanced both adsorption and diffusion of K-ions within the Co-MOF nanocrystals, hence improving the electrochemical performance of the Co-MOF-rGO hybrid. Decreased K-ion migration barrier was also found in a tertiary hierarchical structure of carbon encapsulated ZnS nanorods wrapped in the rGO network (ZSC@C@rGO) [102]. The carbon coated ZnS nanorods were embedded in the rGO network through interfacial connection, which could increase the electronic conductivity, buffer the volume variation during K-ion intercalation/deintercalation, and prevent self-agglomeration of the dendritic-like ZnS (figure 8(d)). A low

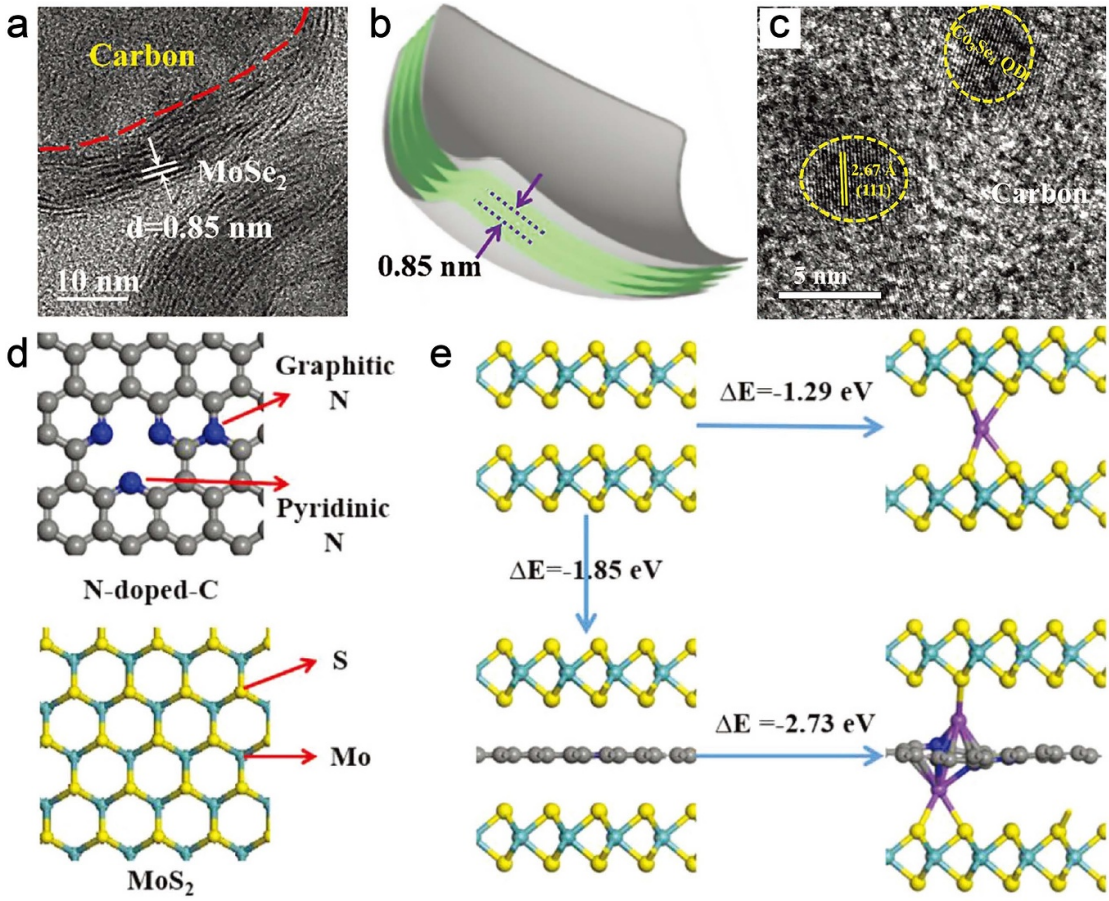

Figure 7. (a) HRTEM image and (b) cross-sectional schematic of $MoSe_2$/C core/shell nanostructures. [92] John Wiley & Sons. [© 2018 WILEY-VCH Verlag GmbH & Co. KGaA, Weinheim]. (c) HRTEM image of Co_3Se_4 QDs encapsulated by N-doped carbon. [100] John Wiley & Sons. [© 2021 WILEY-VCH Verlag GmbH & Co. KGaA, Weinheim]. (d) The optimised ball-and-stick model of N-doped graphene with pyridinic to graphitic N ratio of 3 and the ball-and-stick model of the MoS_2 monolayer; (e) K adsorption in MoS_2/MoS_2 and MoS_2/N-doped-C/MoS_2 interlayer with the formation energies. Green, yellow, black, blue, and purple balls represent Mo, S, C, N, and K atoms, respectively. [98] John Wiley & Sons. [© 2018 WILEY-VCH Verlag GmbH & Co. KGaA, Weinheim].

barrier of K-ion migration in the interphase of ZnS/C was indicated by the NEB calculations in figure 8(e), because K-ion simultaneously interacted with C and ZnS to stabilise the transition state during the reaction. With this interphase, a high capacity of 330 mAh g^{-1} was obtained at 50 mA g^{-1} after 100 cycles.

4.2. Interphases within anode materials

Apart from the interphases formed by a coating layer on anode materials, interphases within anode materials are equally important and should receive more attention in future research on PIBs, because the heterogeneity of the interphases can result in synergetic effects that are beneficial for K-ion migration and cannot be obtained from a carbon interphase on anode materials.

A heterogeneous mixture with rich boundaries is considered as an effective approach for efficient potassium storage, as a built-in electric field can be formed at the heterogeneous interphase and the electronic properties can be improved by modifying the surface reaction kinetics, thus significantly accelerating charge transport [39, 103]. A face-to-face $CoSe_2$/$FeSe_2$@C heterojunction with rich vacancies and low lattice misfits was controllably tuned by Qin *et al* [37]. On the one hand, the semi-coherent $CoSe_2$/$FeSe_2$ phase boundary and vacancies, which was confirmed by the high angle annular dark-field scanning transmission electron microscopy (HAADF-STEM), caused the two individual planes of $CoSe_2$/$FeSe_2$ to form a staggered angle of 20.48° with a low lattice misfit of 12.07% (figure 9(a)). The unique structure with rich defects afforded abundant active sites and ensured a high pseudocapacitance contribution, which shortened the transport pathways of K-ions and accelerated the reaction kinetics. This was suggested by the high *b*-values (>0.75, figure 9(b)) calculated from the CV curves and the capacitive-controlled electrochemical behaviours at the $CoSe_2$/$FeSe_2$ heterojunctions, accounting for 67% of overall energy storage at a scan rate of 0.5 mV s^{-1}. On the other hand, the significantly enhanced charge transfer from $CoSe_2$ to $FeSe_2$ was a result of the built-in electric field between the two materials. The built-in

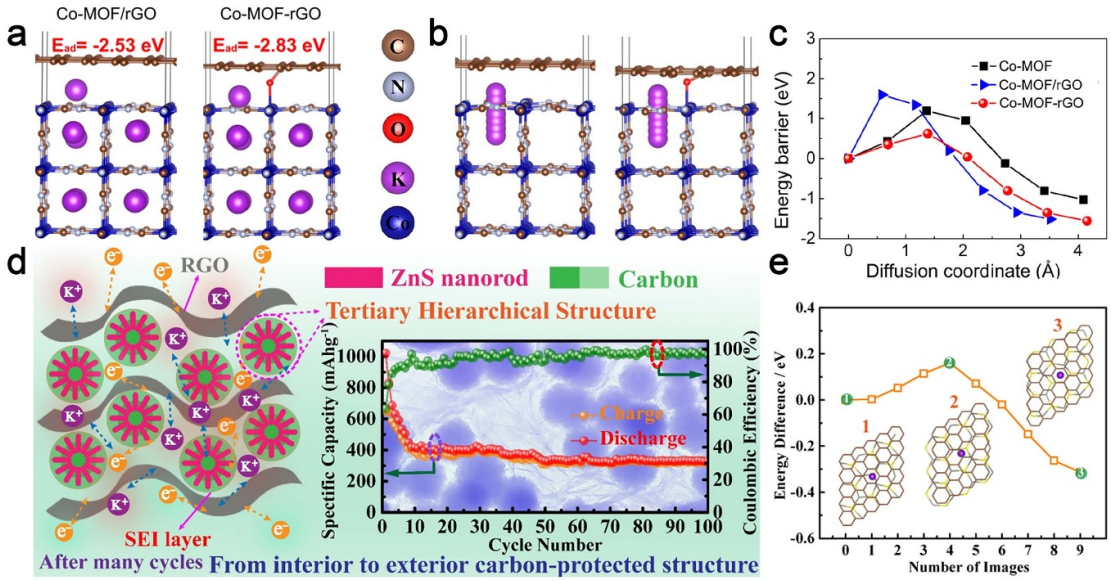

Figure 8. (a) Most stable K atom adsorption on the Co-MOF/rGO composite and the Co-MOF-rGO hybrid and the corresponding adsorption energy; (b) side views of various trajectories from the surface and/or the interface to the pore channel of the Co-MOF/rGO composite (left) and Co-MOF-rGO hybrid (right); (c) energy barrier of K-ion diffusion within the Co-MOF/rGO composite and the Co-MOF-rGO hybrid. Reprinted with permission from [101]. Copyright (2020) American Chemical Society. (d) Schematic illustration of ZSC@C@rGO after many cycles and cycling performance of the ZSC@C@rGO at 50 mA g^{-1} in 0.01–2.5 V; (e) migration barrier of K-ions within the interphase of ZnS/C. Reprinted with permission from [102]. Copyright (2019) American Chemical Society.

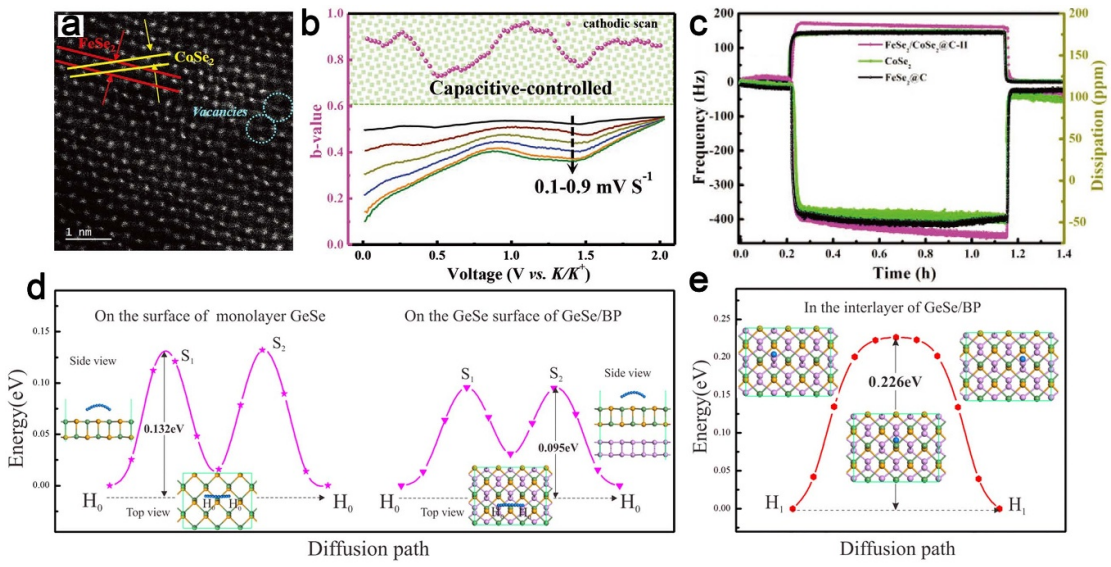

Figure 9. (a) HAADF-STEM image of the $CoSe_2/FeSe_2$ heterojunction structure; (b) *b*-values calculated by the cathodic scan for the $CoSe_2/FeSe_2$@C-II electrode; (c) EQCM frequency response of $CoSe_2/FeSe_2$@C-II, $CoSe_2$, and $FeSe_2$@C. [37] John Wiley & Sons. [© 2021 WILEY-VCH Verlag GmbH & Co. KGaA, Weinheim]. (d) Diffusion energy barrier of one K atom diffusion on monolayer GeSe and the GeSe surface of GeSe/BP; (e) energy barrier of one K atom diffusion in the interlayer of GeSe/BP. Reprinted with permission from [108]. Copyright (2019) American Chemical Society.

electric field speeded up ion diffusion and effectively reduced the activation barrier of charge transfer. The K-ion adsorption energy of $CoSe_2/FeSe_2$ interphase was calculated to be −1.85 eV, significantly higher than −0.55 eV of $CoSe_2$ and −1.21 eV of $FeSe_2$. Electrochemical quartz crystal microbalance (EQCM) frequency response indicated fully recoverable viscoelastic and mass changes of $CoSe_2$–$FeSe_2$@C (figure 9(c)). This indicated the acceleration of reversible K-ion migration by coulombic forces in the built-in electric field of the $FeSe_2/CoSe_2$ interphase [99, 104]. The interphase enabled by the van der Waals forces between two-dimensional (2D) heterojunctions is free of trapped contaminants and not being restrained by lattice matching [105–107]. Zhang *et al* carried out a theoretical investigation of GeSe/BP van der Waals

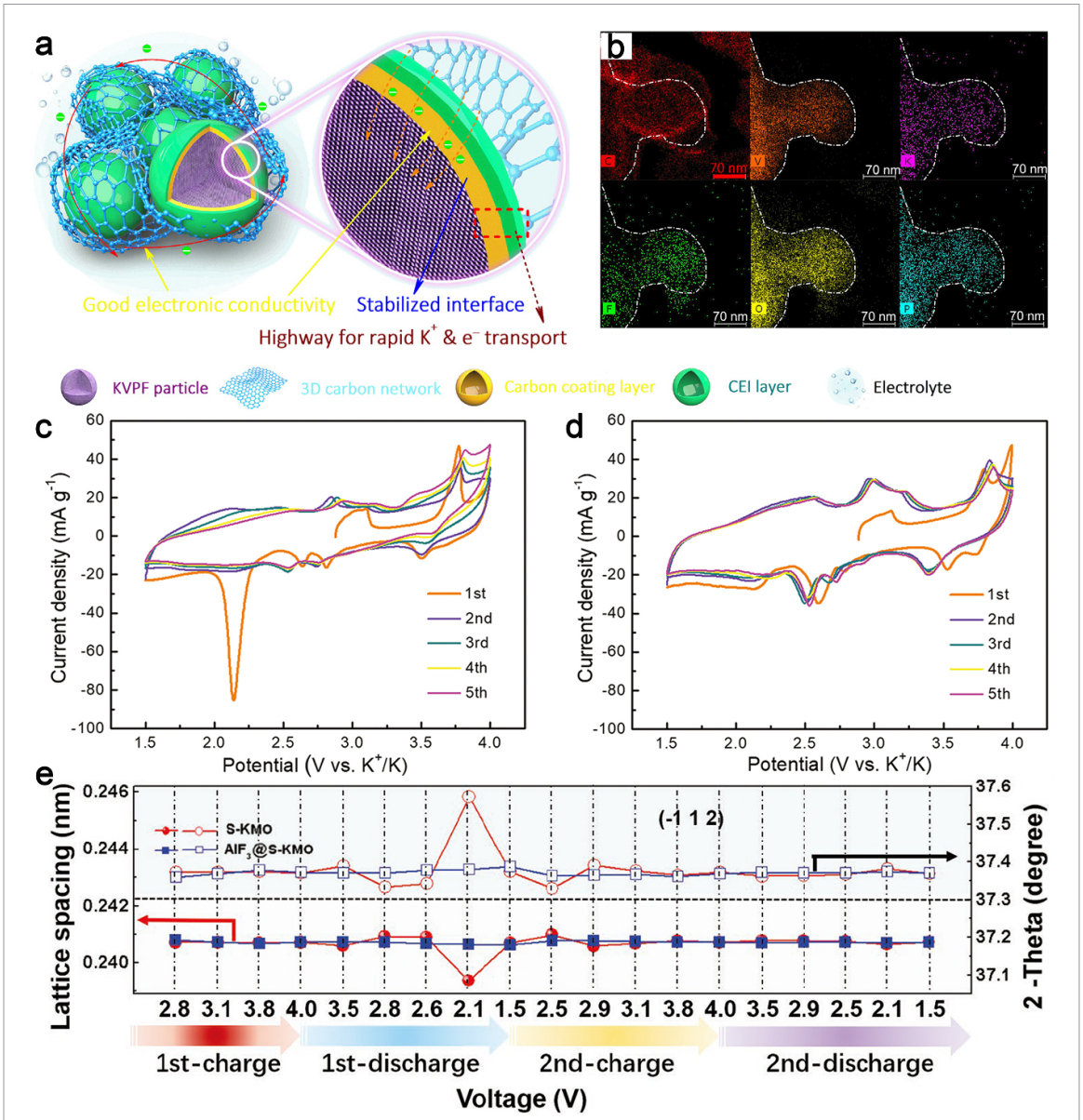

Figure 10. (a) Schematic diagram for the interphase change of the $KVPO_4F$@3D carbon composite during the repeated charge–discharge process; (b) EDS mappings of the disassembled $KVPO_4F$@3D carbon electrode showing the distribution of C, K, V, P, O, and F elements. Reprinted from [114], Copyright (2020), with permission from Elsevier. (c), (d) CV of the cells with (c) the S-KMO and (d) AlF_3@S-KMO electrodes between 1.5 and 4 V (vs K^+/K) at a scan rate of 0.1 mV s^{-1}; (d) relationship between the lattice spacing and the corresponding XRD peak position at various voltage states of the S-KMO and AlF_3@S-KMO electrodes. [115] John Wiley & Sons. [© 2019 WILEY-VCH Verlag GmbH & Co. KGaA, Weinheim].

heterostructures as K-ion anode materials using the first-principle calculations [108]. The results showed that the van der Waals interaction between BP and GeSe can weaken the K bonding at the GeSe surface (figure 9(d)), and as a result, a low K diffusion barrier of 0.226 eV was calculated in the GeSe/BP interlayer (figure 9(e)). This demonstrated that depotassiation was energetically favourable in the GeSe/BP heterostructure. Lu *et al* successfully synthesised 2D van der Waals heterostructure of Bi- and Sb-based oxychloride nanosheets well dispersed on rGO nanosheets. The heterostructure used as an anode for PIB integrated the advantages of the two types of nanosheets and exhibited exceptional electrochemical performance [109].

5. Interphases in composite cathodes

As previously discussed, a CEI layer is formed on the surface of cathode materials to stabilise the electrochemical reactions occurring in the materials [14]. Surface modification of cathodes with an additional interphase layer can further strengthen the electrochemical stability of the cathode [110–113]. Lu *et al* obtained a stable potassium vanadium fluorophosphate ($KVPO_4F$) cathode by forming a protective

carbon coating layer on the $KVPO_4F$ particles [114]. Being different from the conventional roles of keeping structural integrity against volume change, the protection layer in this work plays an important role in preventing the chemical corrosion of the cathode. During cycling, the hydrolysis of KPF_6 in the electrolyte can produce HF, which would corrode the CEI layer and cause a serious decomposition of $KVPO_4F$. Subsequently, lattice defects would be generated on the surface of the $KVPO_4F$ particles, thus increasing the impedance of local charge transfer. With the carbon coating layer, the direct contact between the $KVPO_4F$ particles and the electrolyte was avoided (figure 10(a)), which in turn suppressed the HF corrosion of $KVPO_4F$. The energy dispersive spectroscopy (EDS) mappings in figure 10(b) outlined the $KVPO_4F$ core with the distribution of F, P, V, O and K. The excessive distribution area of the C element proved that the carbon coating layer protected the $KVPO_4F$ core from external attack.

Wang *et al* synthesised $K_{1.39}Mn_3O_6$ microspheres with a 3.1 nm amorphous AlF_3 coating layer (AlF_3@S-KMO) [115]. The strong peak at 2.14 V in the first cathodic CV scan suggested an excessive insertion of K-ions into the K-deficient phase of the uncoated S-KMO cathode (figure 10(c)), and the peak diminished in the following cycles, signalling an irreversible K-ion extraction process. This was in accordance with the rapid electrolyte decomposition during cycling, observed from a continuous increase of peak intensity in the high operating voltage range. In comparison, the AlF_3 coating resulted in the overlapped and well-maintained CV curves of the AlF_3@S-KMO cathode (figure 10(d)). The evolution of lattice spacing at various voltage states were further evaluated by the x-ray diffraction (XRD) measurements to obtain insights into the structural stability of S-KMO and AlF_3@S-KMO electrodes. As shown in figure 10(e), S-KMO underwent a more significant change in the lattice spacing than in AlF_3@S-KMO, especially with the large increase in the crystal plane distance of (−1 1 2) at ∼2.1 V, which was consistent with the strong cathodic CV peak. This suggested the alleviated structural change of S-KMO with AlF_3 surface coating upon K-ion extraction and insertion.

6. Conclusions and perspectives

PIBs offer a cost-effective and sustainable alternative to LIBs, with substantial potential in large-scale energy storage scenarios and showing prospects for mobile energy-dense applications. Two-phase interphases exist throughout PIBs and play an important role in charge transfer, reaction kinetics and electrochemical stability within the battery. Construction and preservation of favourable interphases are crucial for obtaining ideal battery performance. In this review, we focus on solid–liquid interphases including SEI and CEI and solid–solid interphases in composite anode and cathode, through summarising the characteristics of different interphases and analysing the benefits of forming a robust interphase. Recent research progress on optimising the properties of the interphases is discussed in detail. The development of PIBs has made a considerable progression in the last few years, but there is still a long way towards the practical use of PIBs. We put forward our views on the further study of the interphases in PIBs.

(a) The composition and elemental distribution of the SEI determine its structural and electrochemical stability, ionic transport, and long-term durability. Although researchers have caught a glimpse of the structure of the SEI, direct information on the chemical composition of the SEI cannot be obtained with the technological limitation of conventional characterisation techniques such as XPS, scanning electron microscope (SEM) and TEM. It calls for the use of advanced characterisation techniques to probe the chemical composition of SEI in PIBs both in detail and truthfully. The techniques include (1) cryo-TEM to avoid electron radiation damage to the SEI, (2) atom probe tomography and x-ray computed tomography to visualise the 3D distribution of atoms in the SEI and surface morphology of the SEI, respectively, and (3) neutron diffraction for non-destructive profiling of elemental distribution the depth direction. For instance, cryogenic-TEM provides direct observation of crystal structures of inorganic components within the SEI, offering precise information on chemical composition, crystalline structure, and grain boundaries [116]. Meanwhile, neutron diffraction is more suitable for studying organic components in the SEI due to its high sensitivity to lighter elements. In addition, the search for reliable electrolytes with an appropriate combination of solvents, salts and additives is worthy of continuous efforts. It is a practical approach to prepare electrolytes that aid the formation of a strong SEI layer with not only a high content of inorganic components but also a desirable distribution of inorganic/organic components. There are many open questions, such as which components are more conductive and whether K-ions migrate primarily through lattices or grain boundaries, are waiting for an answer.

(b) The influence of binder on the SEI layer formation and its stability has been rarely studied for PIBs. The nature of functional groups in binders can accelerate or restrain the growth of the SEI layer due to the formation of HF/oxide layer which determines the extent of electrolyte decomposition. Hence, investigation on the influence of different binders, such as poly(acrylic acid) (PAA), carboxymethyl cellulose

(CMC), and PVDF, and self-healing and conductive binders on the SEI layer formation will provide a further understanding of the factors influencing the SEI formation, especially for conversion and alloy-based anodes.

(c) CEI is formed mainly by the electrolyte oxidation on the cathode surface when the electric potential is sufficiently high [117]. The formation of CEI can prevent the degradation and pulverisation of the cathode and CEI can be as important as SEI in a battery cell; however, CEI has received less attention compared to SEI in PIBs. Therefore, understanding the constituents of the CEI formed in various electrolytes and electrochemical windows is urgently needed not only because the hunt for high-voltage cathode materials is among one of the most key aspects to enhance energy density of any type of ion batteries, but also the fact that the close electrochemical potential of K to Li and the electrochemical activity of K further raises the demand of high-voltage cathode materials. In the meantime, efforts are required to investigate how to form a robust CEI on reactive cathodes through, for example, electrolyte engineering, surface modification of the cathode, or an artificial surface layer on the cathode, to improve the performance of the cathode. At present, stabilising a CEI on high-voltage cathodes remains a challenge for PIBs due to vigorous side reactions in the highly oxidative environment. Strategies developed in LIBs, such as using highly fluorinated solvents [118, 119] or those with a cyclic structure [120] as well as interfacial modification [121], might be effective.

(d) It has been discussed in this review that a supportive coating layer can work as an interphase to strengthen electrode structure, suppress side reactions, and accelerate ionic/electronic transport, but an excessive amount of the added layer can decrease the packing density of the electrode, leading to unsatisfactory energy density when thick electrodes are required for practical use; hence, ultra-thin coating layers like FLG might be more favourable. This could be tricky because thin electrodes with a low active mass loading might conceal the actual performance due to an excessive amount of conductive carbon additives and binders would minimise the effect of charge transfer and volume changes, which also calls for the tests to verify the practicality of various coating strategies on high-loading electrodes. 2D heterostructures are another materials aspect that is worth exploring for high-performance electrodes of next-generation PIBs. Within a 2D heterostructured electrode, charge transfer can be accelerated at the interphase to maximise power density and new electrochemical processes may be triggered by interphase-induced strain [109]. How to control the stacking of 2D heterostructure layers by adjusting interlayer van der Waals forces might have the potential to deliver unexpected results in terms of facilitating easy K-ion intercalation and fast K-ion movement [108].

Overall, solid–liquid and solid–solid interphases are crucial and complicated issues about PIBs. At present, it is still in a preliminary stage of understanding the fundamentals and evolvement of interphases as well as developing effective strategies to improve the properties of interphases and the resulting performance of electrochemical K storage. There exists an urgent need for advanced *in situ* and *operando* characterisations, a concurrent study of electrochemical K plating/stripping, and consistent consulting between all cell components to push forward the future development of PIBs.

Data availability statement

No new data were created or analysed in this study.

Acknowledgments

Y X acknowledges the support by the Engineering and Physical Sciences Research Council (EP/V000152/1), the Leverhulme Trust (RPG-2021-138), and the Royal Society (RGS\R2\212324). Y H acknowledges the financial support from the China Scholarship Council (CSC).

ORCID iD

Yang Xu https://orcid.org/0000-0003-0177-6348

References

[1] Sovacool B K, Schmid P, Stirling A, Walter G and MacKerron G 2020 Differences in carbon emissions reduction between countries pursuing renewable electricity versus nuclear power *Nat. Energy* **5** 928–35

[2] Vo D H, Vo A T, Ho C M and Nguyen H M 2020 The role of renewable energy, alternative and nuclear energy in mitigating carbon emissions in the CPTPP countries *Renew. Energy* **161** 278–92

[3] Liu Y, Ge Z, Sun Z, Zhang Y, Dong C, Zhang M, Li Z and Chen Y 2020 A high-performance energy storage system from sphagnum uptake waste LIBs with negative greenhouse-gas emission *Nano Energy* **67** 104216
[4] Shi X, Huo X, Ma Y, Pan Z and An L 2020 Energizing fuel cells with an electrically rechargeable liquid fuel *Cell Rep. Phys. Sci.* **1** 100102
[5] Lee J *et al* 2018 Reversible Mn^{2+}/Mn^{4+} double redox in lithium-excess cathode materials *Nature* **556** 185–90
[6] Han Y, Ye L, Boateng B, Sun Q, Zhen C, Chen N, Shi X, Dickerson J H, Li X and He W 2019 Direct electrophoretic deposition of an ultra-strong separator on an anode in a surfactant-free colloidal system for lithium ion batteries *J. Mater. Chem.* A **7** 1410–7
[7] Jung W, Jeong J, Kim J and Chang D 2020 Optimization of hybrid off-grid system consisting of renewables and Li-ion batteries *J. Power Sources* **451** 227754
[8] Lu Y, Saroja A P V K, Wei R and Xu Y 2021 Engineering metal selenides for sodium-and potassium-ion batteries *Cell Rep. Phys. Sci.* **2** 100555
[9] Yang C *et al* 2018 Metallic graphene-like VSe_2 ultrathin nanosheets: superior potassium-ion storage and their working mechanism *Adv. Mater.* **30** 1800036
[10] Hwang J Y, Kim J, Yu T Y, Myung S-T and Sun Y-K 2018 Development of P3-$K_{0.69}CrO_2$ as an ultra-high-performance cathode material for K-ion batteries *Energy Environ. Sci.* **11** 2821–7
[11] Ding J, Zhang H, Fan W, Zhong C, Hu W and Mitlin D 2020 Review of emerging potassium-sulfur batteries *Adv. Mater.* **32** 1908007
[12] Moshkovich M, Gofer Y and Aurbach D 2001 Investigation of the electrochemical windows of aprotic alkali metal (Li, Na, K) salt solutions *J. Electrochem. Soc.* **148** E155
[13] Xu Y, Dong H, Zhou M, Zhang C, Wu Y, Li W, Dong Y and Lei Y 2019 Ammonium vanadium bronze as a potassium-ion battery cathode with high rate capability and cyclability *Small Methods* **3** 1800349
[14] Liu S, Kang L and Jun S C 2021 Challenges and strategies toward cathode materials for rechargeable potassium-ion batteries *Adv. Mater.* **33** 2004689
[15] Ma L, Lv Y, Wu J, Xia C, Kang Q, Zhang Y, Liang H and Jin Z 2021 Recent advances in anode materials for potassium-ion batteries: a review *Nano Res.* **14** 4442–70
[16] Pramudita J C, Sehrawat D, Goonetilleke D and Sharma N 2017 An initial review of the status of electrode materials for potassium-ion batteries *Adv. Energy Mater.* **7** 1602911
[17] Rajagopalan R, Tang Y, Ji X, Jia C and Wang H 2020 Advancements and challenges in potassium ion batteries: a comprehensive review *Adv. Funct. Mater.* **30** 1909486
[18] Zhou M, Bai P, Ji X, Yang J, Wang C and Xu Y 2021 Electrolytes and interphases in potassium ion batteries *Adv. Mater.* **33** 2003741
[19] Popovic J 2021 The importance of electrode interfaces and interphases for rechargeable metal batteries *Nat. Commun.* **12** 1–5
[20] Song J, Xiao B, Lin Y, Xu K and Li X 2018 Interphases in sodium-ion batteries *Adv. Energy Mater.* **8** 1703082
[21] Wang H, Zhai D and Kang F 2020 Solid electrolyte interphase (SEI) in potassium ion batteries *Energy Environ. Sci.* **13** 4583–608
[22] Liu W, Liu P and Mitlin D 2020 Review of emerging concepts in SEI analysis and artificial SEI membranes for lithium, sodium, and potassium metal battery anodes *Adv. Energy Mater.* **10** 2002297
[23] Boateng B *et al* 2020 Organosulfur compounds enable uniform lithium plating and long-term battery cycling stability *Nano Lett.* **20** 2594–601
[24] Liu Y, Gao C, Dai L, Deng Q, Wang L, Luo J, Liu S and Hu N 2020 The features and progress of electrolyte for potassium ion batteries *Small* **16** 2004096
[25] Li B, Zhao J, Zhang Z, Zhao C, Sun P, Bai P, Yang J, Zhou Z and Xu Y 2019 Electrolyte-regulated solid-electrolyte interphase enables long cycle life performance in organic cathodes for potassium-ion batteries *Adv. Funct. Mater.* **29** 1807137
[26] Allgayer F, Maibach J and Jeschull F 2022 Comparing the solid electrolyte interphases on graphite electrodes in K and Li half cells *ACS Appl. Energy Mater.* **5** 1136–48
[27] Fan L, Chen S, Ma R, Wang J, Wang L, Zhang Q, Zhang E, Liu Z and Lu B 2018 Ultrastable potassium storage performance realized by highly effective solid electrolyte interphase layer *Small* **14** 1801806
[28] Deng L, Zhang Y, Wang R, Feng M, Niu X, Tan L and Zhu Y 2019 Influence of KPF_6 and KFSI on the performance of anode materials for potassium-ion batteries: a case study of MoS_2 *ACS Appl. Mater. Interfaces* **11** 22449–56
[29] Xing L, Han K, Liu Q, Liu Z, Chu J, Zhang L, Ma X, Bao Y, Li P and Wang W 2021 Hierarchical two-atom-layered WSe_2/C ultrathin crumpled nanosheets assemblies: engineering the interlayer spacing boosts potassium-ion storage *Energy Storage Mater.* **36** 309–17
[30] Tan Q, Zhao W, Han K, Li P, Wang W, He D, Liu Z, Yu Q, Qin M and Qu X 2019 The multi-yolk/shell structure of FeP@ foam-like graphenic scaffolds: strong P–C bonds and electrolyte-and binder-optimization boost potassium storage *J. Mater. Chem.* A **7** 15673–82
[31] Zhang Q, Mao J, Pang W K, Zheng T, Sencadas V, Chen Y, Liu Y and Guo Z 2018 Boosting the potassium storage performance of alloy-based anode materials via electrolyte salt chemistry *Adv. Energy Mater.* **8** 1703288
[32] Zhang Z *et al* 2021 Cathode-electrolyte interphase in lithium batteries revealed by cryogenic electron microscopy *Matter* **4** 302–12
[33] Zhao J *et al* 2021 *In situ* construction of uniform and robust cathode-electrolyte interphase for Li-rich layered oxides *Adv. Funct. Mater.* **31** 2009192
[34] Ji B, Yao W, Zheng Y, Kidkhunthod P, Zhou X, Tunmee S, Sattayaporn S, Cheng H-M, He H and Tang Y 2020 A fluoroxalate cathode material for potassium-ion batteries with ultra-long cyclability *Nat. Commun.* **11** 1–10
[35] Gaberscek M, Moskon J, Erjavec B, Dominko R and Jamnik J 2008 The importance of interphase contacts in Li ion electrodes: the meaning of the high-frequency impedance arc *Electrochem. Solid-State Lett.* **11** A170
[36] Li J, Li W, You Y and Manthiram A 2018 Extending the service life of high-Ni layered oxides by tuning the electrode-electrolyte interphase *Adv. Energy Mater.* **8** 1801957
[37] Shan H *et al* 2021 Controllable heterojunctions with a semicoherent phase boundary boosting the potassium storage of $CoSe_2$/$FeSe_2$ *Adv. Mater.* **33** 2102471
[38] Xia T, Zhang W, Murowchick J, Liu G and Chen X 2013 Built-in electric field-assisted surface-amorphized nanocrystals for high-rate lithium-ion battery *Nano Lett.* **13** 5289–96
[39] Ni J, Sun M and Li L 2019 Highly efficient sodium storage in iron oxide nanotube arrays enabled by built-in electric field *Adv. Mater.* **31** 1902603
[40] Wu Z, Zou J, Shabanian S, Golovin K and Liu J 2022 The roles of electrolyte chemistry in hard carbon anode for potassium-ion batteries *Chem. Eng. J.* **427** 130972
[41] Wang L *et al* 2019 Identifying the components of the solid-electrolyte interphase in Li-ion batteries *Nat. Chem.* **11** 789–96

[42] Mogensen R, Brandell D and Younesi R 2016 Solubility of the solid electrolyte interphase (SEI) in sodium ion batteries *ACS Energy Lett.* **1** 1173–8
[43] Li Y, Lu Y, Adelhelm P, Titirici M-M and Hu Y-S 2019 Intercalation chemistry of graphite: alkali metal ions and beyond *Chem. Soc. Rev.* **48** 4655–87
[44] Wang H *et al* 2019 A depth-profiling study on the solid electrolyte interface: bis (fluorosulfuryl) imide anion toward improved K^+ storage *ACS Appl. Energy Mater.* **2** 7942–51
[45] Gu X *et al* 2021 A CoSe-C@ C core-shell structure with stable potassium storage performance realized by an effective solid electrolyte interphase layer *J. Mater. Chem.* A **9** 11397–404
[46] Du X and Zhang B 2021 Robust solid electrolyte interphases in localized high concentration electrolytes boosting black phosphorus anode for potassium-ion batteries *ACS Nano* **15** 16851–60
[47] Zhou L *et al* 2020 Electrolyte engineering enables high stability and capacity alloying anodes for sodium and potassium ion batteries *ACS Energy Lett.* **5** 766–76
[48] Ma L, Li J, Wu T, Sun P, Tan S, Wang H, Xie W, Pan L, Yamauchi Y and Mai W 2021 Re-oxidation reconstruction process of solid electrolyte interphase layer derived from highly active anion for potassium-ion batteries *Nano Energy* **87** 106150
[49] Du X, Gao Y and Zhang B 2021 Building elastic solid electrolyte interphases for stabilizing microsized antimony anodes in potassium ion batteries *Adv. Funct. Mater.* **31** 2102562
[50] Tong Z, Tian S, Wang H, Shen D, Yang R and Lee C-S 2020 Tailored redox kinetics, electronic structures and electrode/electrolyte interfaces for fast and high energy-density potassium-organic battery *Adv. Funct. Mater.* **30** 1907656
[51] Zhang X, Meng J, Wang X, Xiao Z, Wu P and Mai L 2021 Comprehensive insights into electrolytes and solid electrolyte interfaces in potassium-ion batteries *Energy Storage Mater.* **38** 30–49
[52] Jian Z, Luo W and Ji X 2015 Carbon electrodes for K-ion batteries *J. Am. Chem. Soc.* **137** 11566–9
[53] Hosaka T, Kubota K, Hameed A S and Komaba S 2020 Research development on K-ion batteries *Chem. Rev.* **120** 6358–466
[54] Lei Y, Han D, Dong J, Qin L, Li X, Zhai D, Li B, Wu Y and Kang F 2020 Unveiling the influence of electrode/electrolyte interface on the capacity fading for typical graphite-based potassium-ion batteries *Energy Storage Mater.* **24** 319–28
[55] Zhang W, Wu Z, Zhang J, Liu G, Yang N-H, Liu R-S, Pang W K, Li W and Guo Z 2018 Unraveling the effect of salt chemistry on long-durability high-phosphorus-concentration anode for potassium ion batteries *Nano Energy* **53** 967–74
[56] Zhang W, Liu Y and Guo Z 2019 Approaching high-performance potassium-ion batteries via advanced design strategies and engineering *Sci. Adv.* **5** eaav7412
[57] Gao Y, Du X, Hou Z, Shen X, Mai Y-W, Tarascon J-M and Zhang B 2021 Unraveling the mechanical origin of stable solid electrolyte interphase *Joule* **5** 1860–72
[58] Fan L, Ma R, Zhang Q, Jia X and Lu B 2019 Graphite anode for a potassium-ion battery with unprecedented performance *Angew. Chem.* **131** 10610–5
[59] Liu S, Mao J, Zhang L, Pang W K, Du A and Guo Z 2021 Manipulating the solvation structure of nonflammable electrolyte and interface to enable unprecedented stability of graphite anodes beyond 2 years for safe potassium-ion batteries *Adv. Mater.* **33** 2006313
[60] Wang H, Yu D, Wang X, Niu Z, Chen M, Cheng L, Zhou W and Guo L 2019 Electrolyte chemistry enables simultaneous stabilization of potassium metal and alloying anode for potassium-ion batteries *Angew. Chem.* **131** 16603–7
[61] Zhou L *et al* 2021 Electrolyte-mediated stabilization of high-capacity micro-sized antimony anodes for potassium-ion batteries *Adv. Mater.* **33** 2005993
[62] Liu S, Mao J, Zhang Q, Wang Z, Pang W K, Zhang L, Du A, Sencadas V, Zhang W and Guo Z 2020 An intrinsically non-flammable electrolyte for high-performance potassium batteries *Angew. Chem., Int. Ed.* **59** 3638–44
[63] Yamada Y, Furukawa K, Sodeyama K, Kikuchi K, Yaegashi M, Tateyama Y and Yamada A 2014 Unusual stability of acetonitrile-based superconcentrated electrolytes for fast-charging lithium-ion batteries *J. Am. Chem. Soc.* **136** 5039–46
[64] Hui J, Schorr N B, Pakhira S, Qu Z, Mendoza-Cortes J L and Rodríguez-López J 2018 Achieving fast and efficient K^+ intercalation on ultrathin graphene electrodes modified by a Li^+ based solid-electrolyte interphase *J. Am. Chem. Soc.* **140** 13599–603
[65] Su S, Liu Q, Wang J, Fan L, Ma R, Chen S, Han X and Lu B 2019 Control of SEI formation for stable potassium-ion battery anodes by Bi-MOF-derived nanocomposites *ACS Appl. Mater. Interfaces* **11** 22474–80
[66] Wang B, Yuan F, Li W, Wang Q, Ma X, Gu L, Sun H, Xi K, Zhang D and Wang W 2020 Rational formation of solid electrolyte interface for high-rate potassium ion batteries *Nano Energy* **75** 104979
[67] Naylor A J, Carboni M, Valvo M and Younesi R 2019 Interfacial reaction mechanisms on graphite anodes for K-ion batteries *ACS Appl. Mater. Interfaces* **11** 45636–45
[68] Adams R A, Varma A and Pol V G 2018 Mechanistic elucidation of thermal runaway in potassium-ion batteries *J. Power Sources* **375** 131–7
[69] Zeng G, Xiong S, Qian Y, Ci L and Feng J 2019 Non-flammable phosphate electrolyte with high salt-to-solvent ratios for safe potassium-ion battery *J. Electrochem. Soc.* **166** A1217
[70] Liu G, Cao Z, Zhou L, Zhang J, Sun Q, Hwang J-Y, Cavallo L, Wang L, Sun Y-K and Ming J 2020 Additives engineered nonflammable electrolyte for safer potassium ion batteries *Adv. Funct. Mater.* **30** 2001934
[71] Nikitina V A, Kuzovchikov S M, Fedotov S S, Khasanova N R, Abakumov A M and Antipov E V 2017 Effect of the electrode/electrolyte interface structure on the potassium-ion diffusional and charge transfer rates: towards a high voltage potassium-ion battery *Electrochim. Acta* **258** 814–24
[72] Zhang X, Yang Y, Qu X, Wei Z, Sun G, Zheng K, Yu H and Du F 2019 Layered P2-type $K_{0.44}Ni_{0.22}Mn_{0.78}O_2$ as a high-performance cathode for potassium-ion batteries *Adv. Funct. Mater.* **29** 1905679
[73] Deng T, Fan X, Chen J, Chen L, Luo C, Zhou X, Yang J, Zheng S and Wang C 2018 Layered P2-type $K_{0.65}Fe_{0.5}Mn_{0.5}O_2$ microspheres as superior cathode for high-energy potassium-ion batteries *Adv. Funct. Mater.* **28** 1800219
[74] Lei K, Zhu Z, Yin Z, Yan P, Li F and Chen J 2019 Dual interphase layers *in situ* formed on a manganese-based oxide cathode enable stable potassium storage *Chem* **5** 3220–31
[75] Yu D, Wang H, Zhang W, Dong H, Zhu Q, Yang J and Huang S 2021 Unraveling the role of ion-solvent chemistry in stabilizing small-molecule organic cathode for potassium-ion batteries *Energy Storage Mater.* **43** 172–81
[76] Xu Y S, Guo S J, Tao X S, Sun Y-G, Ma J, Liu C and Cao A-M 2021 High-performance cathode materials for potassium-ion batteries: structural design and electrochemical properties *Adv. Mater.* **33** 2100409
[77] Wen B, Deng Z, Tsai P C, Lebens-Higgins Z W, Piper L F J, Ong S P and Chiang Y-M 2020 Ultrafast ion transport at a cathode-electrolyte interface and its strong dependence on salt solvation *Nat. Energy* **5** 578–86

[78] Li L, Liu L, Hu Z, Lu Y, Liu Q, Jin S, Zhang Q, Zhao S and Chou S-L 2020 Understanding high-rate K^+-solvent co-intercalation in natural graphite for potassium-ion batteries *Angew. Chem.* **132** 13017–24

[79] Niu X, Zhang Y, Tan L, Yang Z, Yang J, Liu T, Zeng L, Zhu Y and Guo L 2019 Amorphous $FeVO_4$ as a promising anode material for potassium-ion batteries *Energy Storage Mater.* **22** 160–7

[80] Liu Y, Deng Q, Li Y, Li Y, Zhong W, Hu J, Ji X, Yang C, Lin Z and Huang K 2021 CoSe@ N-doped carbon nanotubes as a potassium-ion battery anode with high initial coulombic efficiency and superior capacity retention *ACS Nano* **15** 1121–32

[81] Yang F, Hao J, Long J, Liu S, Zheng T, Lie W, Chen J and Guo Z 2021 Achieving high-performance metal phosphide anode for potassium ion batteries via concentrated electrolyte chemistry *Adv. Energy Mater.* **11** 2003346

[82] Yang H, Xu R, Yao Y, Ye S, Zhou X and Yu Y 2019 Multicore-shell Bi@ N-doped carbon nanospheres for high power density and long cycle life sodium- and potassium-ion anodes *Adv. Funct. Mater.* **29** 1809195

[83] Zheng J, Yang Y, Fan X, Ji G, Ji X, Wang H, Hou S, Zachariah M R and Wang C 2019 Extremely stable antimony-carbon composite anodes for potassium-ion batteries *Energy Environ. Sci.* **12** 615–23

[84] Wang L *et al* 2019 Graphite as a potassium ion battery anode in carbonate-based electrolyte and ether-based electrolyte *J. Power Sources* **409** 24–30

[85] Huang J, Lin X, Tan H and Zhang B 2018 Bismuth microparticles as advanced anodes for potassium-ion battery *Adv. Energy Mater.* **8** 1703496

[86] Chen K T and Tuan H Y 2020 Bi-Sb nanocrystals embedded in phosphorus as high-performance potassium ion battery electrodes *ACS Nano* **14** 11648–61

[87] Zhao Y, Zhu J, Ong S J H, Yao Q, Shi X, Hou K, Xu Z J and Guan L 2018 High-rate and ultralong cycle-life potassium ion batteries enabled by *in situ* engineering of yolk-shell FeS_2@C structure on graphene matrix *Adv. Energy Mater.* **8** 1802565

[88] Wang S, Xiong P, Guo X, Zhang J, Gao X, Zhang F, Tang X, Notten P H L and Wang G 2020 A stable conversion and alloying anode for potassium-ion batteries: a combined strategy of encapsulation and confinement *Adv. Funct. Mater.* **30** 2001588

[89] Zhang L, Wang W, Lu S and Xiang Y 2021 Carbon anode materials: a detailed comparison between Na-ion and K-ion batteries *Adv. Energy Mater.* **11** 2003640

[90] Li D, Zhang J, Ahmed S M, Suo G, Wang W, Feng L, Hou X, Yang Y, Ye X and Zhang L 2020 Amorphous carbon coated SnO_2 nanohseets on hard carbon hollow spheres to boost potassium storage with high surface capacitive contributions *J. Colloid Interface Sci.* **574** 174–81

[91] Ahmed S M, Suo G, Wang W A, Xi K and Iqbal S B 2021 Improvement in potassium ion batteries electrodes: recent developments and efficient approaches *J. Energy Chem.* **62** 307–37

[92] Wang W, Jiang B, Qian C, Lv F, Feng J, Zhou J, Wang K, Yang C, Yang Y and Guo S 2018 Pistachio-shuck-like $MoSe_2$/C core/shell nanostructures for high-performance potassium-ion storage *Adv. Mater.* **30** 1801812

[93] Zhang W, Pang W K, Sencadas V and Guo Z 2018 Understanding high-energy-density Sn_4P_3 anodes for potassium-ion batteries *Joule* **2** 1534–47

[94] Han K *et al* 2019 High-throughput fabrication of 3D N-doped graphenic framework coupled with Fe_3C@ porous graphite carbon for ultrastable potassium ion storage *Energy Storage Mater.* **22** 185–93

[95] Zhao Y *et al* 2020 *In situ* formation of hierarchical bismuth nanodots/graphene nanoarchitectures for ultrahigh-rate and durable potassium-ion storage *Small* **16** 1905789

[96] Cheng N, Zhao J, Fan L, Liu Z, Chen S, Ding H, Yu X, Liu Z and Lu B 2019 Sb-MOFs derived Sb nanoparticles@ porous carbon for high performance potassium-ion batteries anode *Chem. Commun.* **55** 12511–4

[97] Liu D, Huang X, Qu D, Zheng D, Wang G, Harris J, Si J, Ding T, Chen J and Qu D 2018 Confined phosphorus in carbon nanotube-backboned mesoporous carbon as superior anode material for sodium/potassium-ion batteries *Nano Energy* **52** 1–10

[98] Jia B *et al* 2018 Bamboo-like hollow tubes with MoS_2/N-doped-C interfaces boost potassium-ion storage *Adv. Funct. Mater.* **28** 1803409

[99] Huang H, Cui J, Liu G, Bi R and Zhang L 2019 Carbon-coated $MoSe_2$/MXene hybrid nanosheets for superior potassium storage *ACS Nano* **13** 3448–56

[100] Hussain N, Li M, Tian B and Wang H 2021 Co_3Se_4 quantum dots as an ultrastable host material for potassium-ion intercalation *Adv. Mater.* **33** 2102164

[101] Xiao P, Li S, Yu C, Wang Y and Xu Y 2020 Interface engineering between the metal-organic framework nanocrystal and graphene toward ultrahigh potassium-ion storage performance *ACS Nano* **14** 10210–8

[102] Chu J *et al* 2019 Deeply nesting zinc sulfide dendrites in tertiary hierarchical structure for potassium ion batteries: enhanced conductivity from interior to exterior *ACS Nano* **13** 6906–16

[103] Cao L, Liang X, Ou X, Yang X, Li Y, Yang C, Lin Z and Liu M 2020 Heterointerface engineering of hierarchical Bi_2S_3/MoS_2 with self-generated rich phase boundaries for superior sodium storage performance *Adv. Funct. Mater.* **30** 1910732

[104] Li Y *et al* 2020 Co-construction of sulfur vacancies and heterojunctions in tungsten disulfide to induce fast electronic/ionic diffusion kinetics for sodium-ion batteries *Adv. Mater.* **32** 2005802

[105] Geim A K and Grigorieva I V 2013 van der Waals heterostructures *Nature* **499** 419–25

[106] Anasori B, Lukatskaya M R and Gogotsi Y 2017 2D metal carbides and nitrides (MXenes) for energy storage *Nat. Rev. Mater.* **2** 1–17

[107] Wu L, Zheng J, Wang L, Xiong X, Shao Y, Wang G, Wang J-H, Zhong S and Wu M 2019 PPy-encapsulated SnS_2 nanosheets stabilized by defects on a TiO_2 support as a durable anode material for lithium-ion batteries *Angew. Chem.* **131** 821–5

[108] He C, Zhang J H, Zhang W X and Li T T 2019 GeSe/BP van der Waals heterostructures as promising anode materials for potassium-ion batteries *J. Phys. Chem.* C **123** 5157–63

[109] Wang J, Wang B and Lu B 2020 Nature of novel 2D van der Waals heterostructures for superior potassium ion batteries *Adv. Energy Mater.* **10** 2000884

[110] Zhu Y, Yin Y, Yang X, Sun T, Wang S, Jiang Y-S, Yan J-M and Zhang X-B 2017 Transformation of rusty stainless-steel meshes into stable, low-cost, and binder-free cathodes for high-performance potassium-ion batteries *Angew. Chem., Int. Ed.* **56** 7881–5

[111] Chong S, Wu Y, Liu C, Chen Y, Guo S, Liu Y and Cao G 2018 Cryptomelane-type MnO_2/carbon nanotube hybrids as bifunctional electrode material for high capacity potassium-ion full batteries *Nano Energy* **54** 106–15

[112] Xue Q, Li L, Huang Y, Huang R, Wu F and Chen R 2019 Polypyrrole-modified Prussian blue cathode material for potassium ion batteries via *in situ* polymerization coating *ACS Appl. Mater. Interfaces* **11** 22339–45

[113] Li H, Dong J, Han D, Hu J, Li X, Kang F and Zhai D 2020 Simple synthesis of $K_{0.5}VOPO_4 \cdot 1.5H_2O$/graphene oxide composite as a cathode material for potassium-ion batteries *ACS Appl. Energy Mater.* **4** 445–51

[114] Liu Z, Wang J and Lu B 2020 Plum pudding model inspired $KVPO_4F$@3DC as high-voltage and hyperstable cathode for potassium ion batteries *Sci. Bull.* **65** 1242–51
[115] Zhao S, Yan K, Munroe P, Sun B and Wang G 2019 Construction of hierarchical $K_{1.39}Mn_3O_6$ spheres via AlF_3 coating for high-performance potassium-ion batteries *Adv. Energy Mater.* **9** 1803757
[116] Zachman M J, Tu Z, Choudhury S, Archer L A and Kourkoutis L F 2018 Cryo-STEM mapping of solid-liquid interfaces and dendrites in lithium-metal batteries *Nature* **560** 345–9
[117] Liu P and Mitlin D 2020 Emerging potassium metal anodes: perspectives on control of the electrochemical interfaces *Acc. Chem. Res.* **53** 1161–75
[118] Fan X *et al* 2018 Non-flammable electrolyte enables Li-metal batteries with aggressive cathode chemistries *Nat. Nanotechnol.* **13** 715–22
[119] Zhang Z, Hu L, Wu H, Weng W, Koh M, Redfern P C, Curtiss L A and Amine K 2013 Fluorinated electrolytes for 5 V lithium-ion battery chemistry *Energy Environ. Sci.* **6** 1806–10
[120] Zheng Q, Yamada Y, Shang R, Ko S, Lee Y-Y, Kim K, Nakamura E and Yamada A 2020 A cyclic phosphate-based battery electrolyte for high voltage and safe operation *Nat. Energy* **5** 291–8
[121] Qiu B *et al* 2016 Gas-solid interfacial modification of oxygen activity in layered oxide cathodes for lithium-ion batteries *Nat. Commun.* **7** 1–10